Numerical investigation of shock wave interactions with flexible fiber granular curtains

Peng Wang[1], Jiawei Han[1], Kun Xue[2,*], and Yu Guo[1,**]

[1]*Department of Engineering Mechanics,*

Zhejiang University, Hangzhou, 310027, China

[2]*State Key Laboratory of Explosive Science and Technology,*

Beijing Institute of Technology, Beijing 100081, China

[*]*Corresponding author. Email: xuekun@bit.edu.cn*

[**]*Corresponding author. Email: yguo@zju.edu.cn*

(Dated: October 9, 2025)

Abstract

The interaction between air shock waves and granular materials is fundamental in both natural phenomena and engineering applications. However, the role of particle morphology, particularly that of flexible fibers, remains unclear. Here, we numerically investigate shock-induced dispersal and resistance in dense flexible fiber curtains, using a coupled Discrete Element Method and Computational Fluid Dynamics (DEM–CFD) framework. We find that the dispersal dynamics and shock attenuation are governed by the competition between fiber interlocking and cluster volume fraction (solid volume fraction in a cluster). Low aspect ratio fiber systems, which have high cluster volume fractions, exhibit non-uniform expansion, with instabilities at the downstream interface leading to pronounced granular ejections, resulting in rapid dispersion of the clusters. In contrast, high aspect ratio fiber systems, which possess lower cluster volume fractions, maintain integrity of the clusters for much longer periods due to the fiber interlocking contacts, thereby suppressing the interfacial instabilities. Consequently, stronger resistance to the shock by the fiber cluster is obtained at early stage of the wave propagation for the low aspect ratio fibers, and the stronger shock-resistance occurs at a later stage for the high aspect ratio fibers. Fiber flexibility modulates these behaviors by promoting fiber bending deformation, effectively weakening geometric interlocking and reducing air drag. To describe the time evolution of the fiber curtain expansion, the fiber aspect ratio should be included in scaling law to account for the effect of fiber shape on the air drag. For the very flexible fibers, an effective fiber aspect ratio is required to replace the real fiber aspect ratio in the scaling law, in order to take the effect of large fiber deformation into account. These findings offer a fundamental understanding of the shock-driven multiphase flows and dispersal of the elongated, flexible fibers.

I.   INTRODUCTION

The interaction between shock waves and granular materials is ubiquitous in many critical processes across natural systems and engineering applications. In natural environments, such interactions drive the dynamics of volcanic pyroclastic flows, influencing eruption hazards and ash dispersal [1, 2], and they play an instrumental role in propagation of seismic waves through granular soils during earthquakes, affecting ground stability and infrastructure resilience [3, 4]. In engineering contexts, they are pivotal to explosion mitigation, enhancing

structural safety during blasts [5, 6], as well as to cold spraying processes for advanced coatings [7] and mining safety measures aimed at preventing dust explosions [8]. These diverse applications underscore the necessity of understanding the physics of shock-induced granular flows.

During a shock wave propagates through a granular medium, gas-particle interactions induce wave reflection and transmission, facilitate energy exchange between the gas and solid phases, and drive particle acceleration [9, 10]. These behaviors stem from intricate multi-physics phenomena, including energy conversion, inelastic collisions, and wave scattering. A critical parameter governing these interactions is the solid volume fraction ϕ_0, defined as the ratio of volume of all the solid particles to volume of the space occupied by the bulk granular material. Early experiments on the shock-impacted dilute particle curtains, with ϕ_0 varying from 0.1% to 3%, demonstrated that reflected shock waves emerge only when ϕ_0 exceeds 1% [11]. Subsequent studies, which utilized dense particle curtains packed under gravitational forces [12–15], established correlations between strength of the reflected shock and curtain properties, including ϕ_0 [16], curtain thickness [15], particle size [17], and particle density [14]. Upstream and downstream fronts of a particle curtain subject to the shock impact exhibit markedly distinct behaviors. Within tens of microseconds of the incident shock impinging, the downstream particles initiate motion, and after a short period of delay the upstream particles commence movement at a reduced velocity [12]. Numerical simulations reveal that positive gas velocity gradients and negative pressure gradients occur within the curtain, and the net force from the negative pressure gradient accelerates the downstream particles and the positive gas velocity gradient drives the curtain to expand [13].

The dispersal and expansion of dense particle curtains under shock loading have been systematically analyzed. Scaling laws were developed to relate physical parameters to dimensionless quantities. Ling *et al.* [13] proposed using the time taken for a shock wave to pass through the particle curtain to normalize the time t. Theofanous *et al.* [18] further introduced a pressure-based temporal scaling approach by normalizing the spreading time t against theoretical pressure of the reflected shock, calculated by assuming the particle curtain as a rigid wall. This scaling approach successfully collapsed the early-time data of the particle curtain expansion from their experiments and prior studies [12, 13], despite neglecting the permeability of particle curtain. DeMauro *et al.* [19] advanced this framework using high-speed Particle Image Velocimetry (PIV) measurement, demonstrating that the tran-

sient pressure gradient, which is driven by reflected and transmitted shocks, serves as the primary mechanism governing the curtain expansion and the pressure gradient is strongly dependent on the solid volume fraction. Further, by treating the curtain as a porous screen, DeMauro *et al.* [20] incorporated the solid volume fraction directly into the scaling correlation, which collapsed data across various Mach numbers M_s, solid volume fractions ϕ_0, particle densities and curtain thicknesses for the spherical particles.

Shock-induced particle dispersal is further complicated by mesoscale behaviors such as particle clustering and interfacial instability [21]. Experiments with spherical particles reveal that the localized regions of high ϕ_0, which are usually referred to as clusters, are developed on the downstream side of the curtains [22], accompanied by gas-particle interfacial instabilities that can manifest as sharp, finger-like protrusions of particles [23–25]. The particle ejections, driven by localized momentum transfer, travel at the velocities surpassing the average dispersal velocity, and their characteristics depend on gas-to-particle mass ratio [26, 27]. A higher gas-to-particle mass ratio enhances the interaction between the gas and solid phases, promoting the formation of these mesoscale structures.

Although extensive studies have elucidated these shock-impacted processes for the idealized spherical particles, the role of particle morphology—particularly of flexible fibers with high fiber aspect ratios (AR) and bending deformation compliance—remains largely unexplored. Unlike the spherical particles, elongated and deformable nature of such fibers suggests they exhibit distinct energy dissipation pathways [28] and dispersal behaviors. The flexible fibers with high aspect ratios have different mesoscale behaviors from the spherical particles. The elongated fibers possess the ability to bend, twist, and entangle with their neighbors. These morphological attributes allow significant bulk compressibility and high shear yield strength due to geometric interlocking, in which individual fibers physically interweave and mechanically constrain one another. These distinct features, which are absent in the spherical particle systems, lead to unique packing structures and force transmission mechanisms within the fiber assemblies [29, 30]. Consequently, the presence and strength of the fiber interlocking can potentially modify the particle clustering, alter the interfacial instabilities, and induce anisotropic flow resistance within the shock-dispersed media.

To bridge the knowledge gaps in the interactions between the shock and fiber assemblies, in this work we employ a coupled Discrete Element Method and Computational Fluid Dynamics (DEM-CFD) approach to simulate the processes of shock waves impacting on

4

dense flexible fiber curtains. The effects of fiber properties (including fiber aspect ratio and fiber flexibility) on granular dispersion pattern, cluster formation, and shock attenuation are investigated. At last, a modified scaling law is proposed to describe the time-dependent expansion of the fiber curtains with various fiber aspect ratios and flexibilities.

II. NUMERICAL METHOD

In this work, compressible air-fiber flows are simulated using a coupled DEM-CFD method. The flexible fibers are modelled via a DEM-based bonded sphero-cylinder fiber model, which was developed in the previous work [31, 32]. The air flow is governed by a continuum-based CFD approach, solving the compressible Navier-Stokes equations [33]. Two-way coupling is considered for the gas–fiber interaction. The governing equations of the numerical scheme used in this study are presented below.

A. Bonded sphero-cylinder fiber model

In the present DEM simulations, a flexible fiber is represented by a string of bonded sphero-cylinder elements, and a sphero-cylinder element includes two neighboring spherical nodes connected by a virtual bond as shown in figure 1(a). The motion of a fiber is determined by collective movement of the node spheres, including translational and rotational movement governed by Newton's second law of motion,

$$m_s \frac{\mathrm{d}\boldsymbol{v}_s}{\mathrm{d}t} = \boldsymbol{F}^b + \boldsymbol{F}^c + \boldsymbol{F}_d^b + \boldsymbol{F}_d^c + \boldsymbol{F}^{gs}, \tag{1}$$

and

$$J_s \frac{\mathrm{d}\boldsymbol{\omega}_s}{\mathrm{d}t} = \boldsymbol{M}^b + \boldsymbol{M}^c + \boldsymbol{M}_d^b + \boldsymbol{M}_d^c, \tag{2}$$

in which $\boldsymbol{v}_s$ and $\boldsymbol{\omega}_s$ are the translational and angular velocity vectors, respectively, of the node sphere with mass m_s and moment of inertia J_s. The translational movement of the node sphere is driven by the contact force $\boldsymbol{F}^c$ between two contacted sphero-cylinders, bond force $\boldsymbol{F}^b$ generated from virtual bond to resist the elastic deformation of the fiber, contact damping forces $\boldsymbol{F}_d^c$ and bond damping forces $\boldsymbol{F}_d^b$. The rotational movement is induced by the moments $\boldsymbol{M}^c$, $\boldsymbol{M}^b$, $\boldsymbol{M}_d^c$ and $\boldsymbol{M}_d^b$ due to the contact forces, bond forces/moments, contact damping forces, and bond damping forces/moments, respectively.
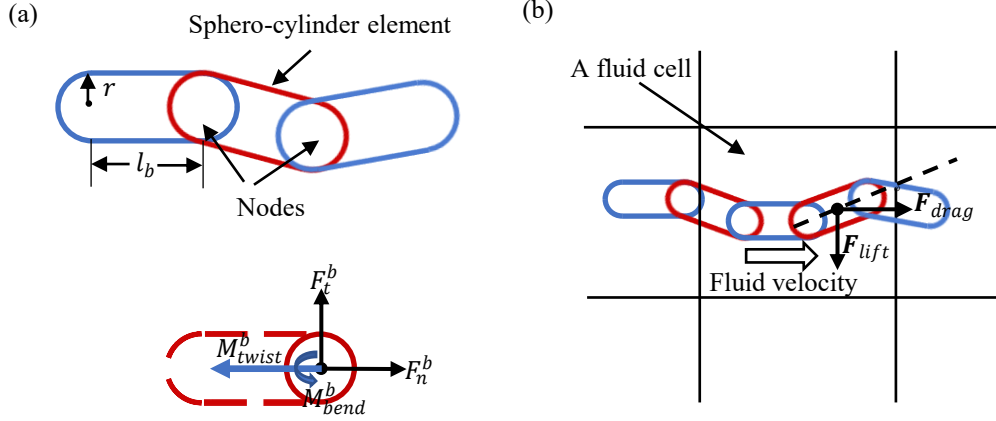
5

FIG. 1. (a) A sketch of flexible model and an illustration of bond forces and moments exerted on a node sphere. (b) An illustration of drag force and lift force exerted on a sphero-cylinder element.

The bond forces $\boldsymbol{F}^b$, including normal bond force $\boldsymbol{F}_n^b$ and tangential bond force $\boldsymbol{F}_t^b$, and bond moments $\boldsymbol{M}^b$, including twist moment $\boldsymbol{M}_{twist}^b$ and bending moment $\boldsymbol{M}_{bend}^b$, as illustrated in figure 1(a), are functions of bond deformation, which is described by the relative displacements between two connected node spheres. Hence, the normal and tangential bond forces $\boldsymbol{F}_n^b$ and $\boldsymbol{F}_t^b$ are expressed as linear function of normal and tangential displacements $\boldsymbol{\Delta}_n^b$ and $\boldsymbol{\Delta}_t^b$, respectively,

$$\boldsymbol{F}_n^b = \frac{E_b A}{l_b}\boldsymbol{\Delta}_n^b = K_n^b \boldsymbol{\Delta}_n^b, \tag{3}$$

and

$$\boldsymbol{F}_t^b = \frac{G_b A}{l_b}\boldsymbol{\Delta}_t^b = K_t^b \boldsymbol{\Delta}_t^b. \tag{4}$$

The bond twist moment $\boldsymbol{M}_{twist}^b$ and the bond bending moment $\boldsymbol{M}_{bend}^b$ are computed incrementally for each time step dt based on the relative twisting angular velocity $\dot{\boldsymbol{\theta}}_{twist}$ and relative bending angular velocity $\dot{\boldsymbol{\theta}}_{bend}$ between two bond-connected node spheres,

$$\mathrm{d}\boldsymbol{M}_{twist}^b = \frac{G_b I_p}{l_b}\dot{\boldsymbol{\theta}}_{twist}\mathrm{d}t = K_{twist}^b \dot{\boldsymbol{\theta}}_{twist}\mathrm{d}t, \tag{5}$$

and

$$\mathrm{d}\boldsymbol{M}_{bend}^b = \frac{E_b I}{l_b}\dot{\boldsymbol{\theta}}_{bend}\mathrm{d}t = K_{bend}^b \dot{\boldsymbol{\theta}}_{bend}\mathrm{d}t. \tag{6}$$

In Eqs. (3)-(6), E_b and G_b ($G_b = \frac{E_b}{2(1+\nu_b)}$ where ν_b is the Poisson's ratio of the bond) are the elastic modulus and shear modulus, respectively, of the bond material; A and l_b are the cross-sectional area and length, respectively, of the bond; $I = \pi r^4/4$ is the area moment

6

of inertia; $I_p = \pi r^4 / 2$ is the polar area moment of inertia, and r is the radius of the fiber. According to Eq. (6), fiber flexibility, indicating the ease for the bending deformation of the fiber, is characterized by the bending modulus E_b: a smaller E_b corresponds to a larger fiber flexibility. Fiber-fiber contacts and fiber-wall contacts are modelled as normal and tangential contact forces, described by the modified Hertz-Mindlin models [32, 34]. Viscous dissipation of energies in the contacts and fiber deformations is considered through contact damping and bond damping forces/moments [32, 34].

The interaction force between air and each sphero-cylinder element, denoted as $\mathbf{F^{gsc}}$, is expressed as [35]

$$\boldsymbol{F}^{gsc} = -V_{sc}\nabla p + V_{sc}\nabla \cdot \boldsymbol{\tau} + \varepsilon_g(\boldsymbol{F}_{\text{drag}} + \boldsymbol{F}_{\text{lift}}) \tag{7}$$

in which V_{sc} is the volume of a sphero-cylinder element, p is the local air pressure, τ is the local viscous stress tensor of the air, ε_g is the local porosity, $\boldsymbol{F}_{\text{drag}}$ and $\boldsymbol{F}_{\text{lift}}$ are the drag and lift forces as shown in figure 1(b), respectively, exerted on the sphero-cylinder element. The interaction force $\boldsymbol{F}^{gsc}$ on each sphero-cylinder element is uniformly distributed to its two constituent spherical nodes, and therefore the air force on each node sphere is given by $\boldsymbol{F}^{gs} = 0.5\boldsymbol{F}^{gsc}$.

B. Equations for compressible air flows

For the air phase, volume-averaged governing equations of mass, momentum, and energy in the Eulerian framework are expressed as follows [17],

$$\frac{\partial(\varepsilon_g \rho_g)}{\partial t} + \nabla \cdot (\varepsilon_g \rho_g \boldsymbol{u}_g) = 0, \tag{8}$$

$$\frac{\partial(\varepsilon_g \rho_g \boldsymbol{u}_g)}{\partial t} + \nabla \cdot (\varepsilon_g \rho_g \boldsymbol{u}_g \boldsymbol{u}_g) = -\nabla p + \nabla \cdot \boldsymbol{\tau} - \frac{\sum_{i=1}^{n_s} \boldsymbol{F}^{gsc}}{V_{cell}}, \tag{9}$$

$$\begin{aligned}\frac{\partial(\varepsilon_g \rho_g E)}{\partial t} + \nabla \cdot (\varepsilon_g \rho_g E \boldsymbol{u}_g) = &-\nabla \cdot (\varepsilon_g p \boldsymbol{u}_g) + \nabla \cdot (\varepsilon_g \boldsymbol{\tau} \cdot \boldsymbol{u}_g) \\ &-\nabla \cdot (\varepsilon_f p \boldsymbol{u}_f) + \nabla \cdot (\varepsilon_f \boldsymbol{\tau} \cdot \boldsymbol{u}_f) \\ &-\frac{\sum_{i=1}^{n_s} \boldsymbol{F}^{gsc} \cdot \boldsymbol{u}_f}{V_{\text{cell}}}.\end{aligned} \tag{10}$$

The velocity, density, and total energy of the air in a fluid cell are denoted as $\boldsymbol{u}_g$, ρ_g, and $E = e + \frac{|\boldsymbol{u}_g|^2}{2}$, where e is the specific internal energy. The mass-averaged velocity vector and

solid volume fraction of the sphero-cylinder elements in a fluid cell are represented by $\boldsymbol{u}_f$ and ε_f, respectively. The pressure p is calculated from the ideal gas equation of state,

$$p = \rho_g R T_g \tag{11}$$

where R is the specific gas constant and T_g is the temperature of the air. The viscous stress tensor $\boldsymbol{\tau}$ has a linear relationship with shear rate for a Newtonian fluid, where the constant of proportionality is the dynamic viscosity of the fluid (the gas), denoted as μ_g. For the solid phase, the solid volume fraction ε_f and mass-averaged solid velocity vector $\boldsymbol{u}_f$ in each fluid cell are determined using a kernel-based averaging method [36]. The volume of each sphero-cylinder element i is distributed to all fluid cells based on the distance between the element and the cell center, and the weight function for the distribution is written as,

$$\omega_{i,m} = \frac{K(|\boldsymbol{x}_i - \boldsymbol{x}_m|/b)}{\sum_{m=1}^{N_c} K(|\boldsymbol{x}_i - \boldsymbol{x}_m|/b)}, \tag{12}$$

where $K(x) = exp(-x^2)$ is a kernel function, $\boldsymbol{x}_i$ and $\boldsymbol{x}_m$ represent the coordinates of the sphero-cylinder element and fluid cell center, respectively, b is the bandwidth (set equal to twice the fluid cell size), and N_c is the total number of the fluid cells, which are optionally limited to those within a specified region to reduce computational cost. The normalization in the denominator ensures that the total solid volume is preserved in the whole field. Given the volume of the sphero-cylinder element i, $V_{sc,i}$, the solid volume fraction ε_f in the fluid cell m of volume V_c can be calculated as,

$$\varepsilon_f = \frac{\sum_{i=1}^{n_p} \omega_{i,m} V_{sc,i}}{V_c} \tag{13}$$

in which n_p is the total number of the sphero-cylinder elements. Similarly, the solid phase velocity vector $\boldsymbol{u}_f$ in the fluid cell m can be obtained as,

$$\boldsymbol{u}_f = \frac{\sum_{i=1}^{n_p} \omega_{i,m} V_{sc,i} \boldsymbol{v}_{e,i}}{\varepsilon_f V_c} \tag{14}$$

in which $\boldsymbol{v}_{e,i}$ is the translational velocity vector of the center of mass of the sphero-cylinder element i.

To account for the combined effects of voidage and particle shape, the drag force on each sphero-cylinder element is modeled using the Di Felice-Hölzer/ Sommerfeld model [37]. According to [38], the drag force $\boldsymbol{F}_{\mathrm{drag}}$ has the expression,

$$\boldsymbol{F}_{\mathrm{drag}} = \frac{1}{2} C_d \rho_g A_\perp \varepsilon_g^2 |\boldsymbol{u}_g - \boldsymbol{v}_e|(\boldsymbol{u}_g - \boldsymbol{v}_e)\varepsilon_g^{-(\chi+1)}, \tag{15}$$

in which $\boldsymbol{v}_e$ is the translational velocity vector of the center of mass of a sphero-cylinder element, $A_\perp$ is the projected area of a sphero-cylinder element on the plane perpendicular to the direction of the relative velocity $\boldsymbol{u}_g - \boldsymbol{v}_e$, and χ represents a function of the element Reynolds number R_e,

$$\chi = 3.7 - 0.65exp\left[\frac{-(1.5 - log_{10}R_e)^2}{2}\right], \tag{16}$$

$$R_e = \frac{\rho_g d_V \varepsilon_g |\boldsymbol{u}_g - \boldsymbol{v}_e|}{\mu_g}, \tag{17}$$

and d_V is the equivalent volume diameter of the fiber. As proposed by [39], the drag coefficient C_d for a sphero-cylinder is written as,

$$C_d = C_{corr}\left[\frac{8}{R_e}\frac{1}{\sqrt{\psi_\perp}} + \frac{16}{R_e}\frac{1}{\sqrt{\psi}} + \frac{3}{\sqrt{R_e}}\frac{1}{\psi^{3/4}} + 0.42 \times 10^{0.4(-\log_{10}\psi)^{0.2}}\frac{1}{\psi_\perp}\right] \tag{18}$$

in which ψ is the sphericity of a sphero-cylinder element, defined as the ratio of the surface area of a volume-equivalent sphere to the surface area of the present sphero-cylinder, and $\psi_\perp$ is the crosswise sphericity, defined as the ratio of the cross-sectional area of the volume equivalent sphere to the projected area of the sphero-cylinder element on the plane perpendicular to the direction of the relative velocity $\boldsymbol{u}_g - \boldsymbol{v}_e$. The two sphericity factors are included in the drag coefficient calculation to consider the effects of the shape and orientation of the sphero-cylinder element. The correction factor C_{corr} is incorporated to consider the effects of air compressibility and is calculated as a function of element Reynolds number R_e and Mach number M_s according to Carlson and Hoglund [40]:

$$C_{corr} = 1 + exp(-\frac{0.427}{M_s^{4.63}} - \frac{3}{R_e^{0.88}}). \tag{19}$$

The lift force $\boldsymbol{F}_{\text{lift}}$ is exerted on a sphero-cylinder element in the direction perpendicular to the relative velocity vector $\boldsymbol{u}_g - \boldsymbol{v}_e$, and it is written in the form,

$$\boldsymbol{F}_{\text{lift}} = \frac{1}{2}C_l\rho_g\frac{\pi}{4}d_V^2\varepsilon_g^2\,|\boldsymbol{u}_g - \boldsymbol{v}_e|^2\,\boldsymbol{n}_{\text{lift}}\varepsilon_g^{-(\chi+1)} \tag{20}$$

in which $\boldsymbol{n}_{\text{lift}}$ is unit vector in the direction of the lift force vector. The lift coefficient is estimated by $C_l = C_d sin^2\varphi cos\varphi$, where φ is the angle between the major axis of the sphero-cylinder and the direction of the relative velocity $\boldsymbol{u}_g - \boldsymbol{v}_e$ [41].
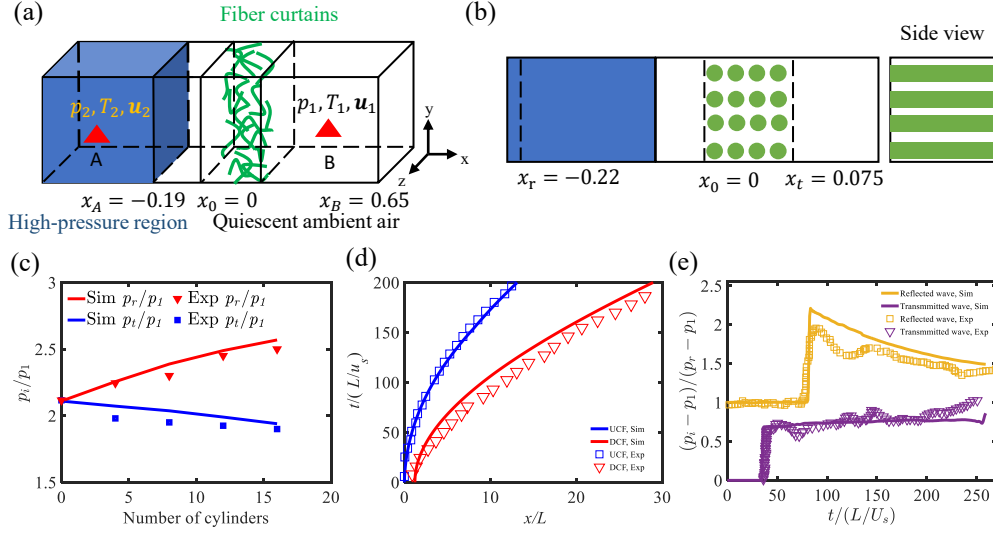
FIG. 2. (a) Numerical model of a shock impacting on a granular curtain of flexible fibers in a long tube. (b) A sketch of the numerical set-up of a shock impacting on an array of elongated cylinders, which mimics the experimental set-up by [42]. (c) A comparison of the pressures of reflected and transmitted waves at the specified positions obtained from the present simulations and previous experiments [42]. (d-e) Validation against the shock-induced granular dispersion experiments of Ling *et al.* [13]: (d) comparison of upstream curtain front (UCF) and downstream curtain front (DCF) between the simulation and experimental results and (e) comparison of reflected and transmitted wave pressure histories at two specified monitoring locations between the simulation and experimental results.

III. NUMERICAL SET-UP AND CODE VALIDATION

In this study, a shock tube configuration is employed to investigate the interaction between high-pressure air shocks and dense fiber curtains, following a design similar to that of [24], as illustrated in Figure 2(a). The computational domain has a rectangular geometry, with transverse dimensions (y and z-directions) of 28 mm and an axial (x-direction) length of 1000 mm in the air inflow direction. The cross-sectional area is therefore $A = 28$ mm $\times$ 28 mm.

The computational domain is divided along the streamwise direction (x-direction) into two regions: an upstream region without fibers and a downstream region containing a curtain

of randomly packed fibers. At the beginning $(t = 0)$, the downstream region is initialized with a quiescent ambient air, representing pre-shock state, at a pressure of $p_1 = 10132$ Pa, a temperature of $T_1 = 298.15$ K, and zero air velocity $u_1 = 0$. The upstream region is initialized with the post-shock state of an incident shock wave at a Mach number of $M_a = 1.1$. The post-shock conditions, determined using the Rankine-Hugoniot relations for an ideal gas, include the air pressure of $p_2 = 126150$ Pa, temperature of $T_2 = 317.51$ K, and air velocity of $u_2 = 55$ m/s in the streamwise x-direction [43]. This initial configuration produces a planar shock wave that propagates from the upstream region into the downstream region, ultimately interacting with the fiber curtain. Non-reflecting boundary conditions are applied on both the upstream and downstream end planes (perpendicular to the x-direction), for which zero gradients are enforced for the air pressure, temperature, and velocity to minimize wave reflections from the streamwise boundaries. The transverse boundaries (perpendicular to the y- and z-directions) are treated as impermeable, no-slip walls for the air flows, and zero gradients are applied for the pressure and temperature on these boundaries. Two positions are chosen to monitor the changes in the air states: Point A is located in the upstream region at $x_A = -0.19$ m to measure the reflected wave pressures p_r and velocity $\boldsymbol{u}_r$, and Point B is located in the downstream region at $x_B = 0.65$ m to measure the transmitted wave pressures p_t and velocity u_t, as depicted in Figure 2(a).

To generate a dense fiber curtain, the following procedure is employed: i) A specified number of fibers are randomly placed within the downstream region $(x > 0)$, with random positions and orientations. Initial overlaps between fibers are avoided; ii) A vertical planar wall (perpendicular to the x-direction) is introduced at the position $x = 0$ (Figure 2(a)); iii) Gravitational forces in the negative x-direction are assigned to the fibers, driving the fibers to pack on the vertical wall at $x = 0$; iv) When the densely-packed fiber curtain remains stable with negligible fiber movement, the gravitational force is deactivated and the planar wall is removed. After this initialization, the shock impact simulation starts in the absence of gravitational forces.

All the fibers have a density of $\rho_f = 880$ kg/m^3, a diameter of $d_f = 0.65$ mm, a friction coefficient of $\mu_f = 0.4$, and a Young's modulus $E_c = 5 \times 10^8$ Pa for the calculation of fiber-fiber contact forces. Following Guo *et al.* [32], a contact damping coefficient of $\beta_c = 7.09 \times 10^{-2}$ and a bond damping coefficient of $\beta_b = 3.35 \times 10^{-2}$ are adopted to model the energy dissipation through fiber-fiber contacts and fiber deformation, respectively. The fiber

aspect ratio, AR, defined as the ratio of length to diameter of a fiber, is varied in the range of $1 \leq AR \leq 20$. Though a fiber can experience tensile/compressive, shearing, twisting, and bending deformations, the bending deformation dominates for the elongated fibers. Thus, the bond bending modulus E_b changes between 5×10^4 Pa and 5×10^8 Pa to achieve different fiber flexibilities in the present simulations.

The bonded sphero-cylinder flexible fiber model has been extensively validated in prior studies, including single-fiber deformation [31] and the mechanical response of fiber assemblies under compression [32]. For compressible air modeling, the open source CFD solver rhoCentralFoam, based on OpenFOAM®, is employed. It is a robust finite-volume solver employing central schemes, specifically designed for high-speed flows. Its reliability is underpinned by extensive validation against a comprehensive suite of canonical test cases, ranging from the one-dimensional shock tube, two-dimensional supersonic flow over a step, supersonic jet density measurements and hypersonic flow over a biconical object [33]. This rigorous validation ensures the solver's suitability for the complex interactions studied herein.

The current coupled DEM-CFD scheme is further validated through two distinct benchmark cases. First, to verify the modeling of the interaction between air flow and elongated cylindrical objects, we simulate a shock impacting an array of fixed cylinders, replicating the experimental setup of Suzuki *et al.* [42] as depicted in Figure 2(b). In the simulations, identical cylinders with an aspect ratio of $AR = 12$ are arranged in regular lattice positions. Their major axes are aligned in the same direction, which is perpendicular to the flow direction. Four configurations of the cylinder arrangement (rows × columns) are considered: 4×1, 4×2, 4×3, and 4×4. Each cylinder is discretized into 11 sphero-cylinder elements with 12 spherical nodes. An incident shock wave at a Mach number of $M_a = 1.4$ is initialized in the domain using the same approach as the simulation illustrated in Figure 2(a).

In the experiments Suzuki *et al.* [42], the pressures of the reflected wave (p_r) and the transmitted wave (p_t) are measured at the locations $x_r = -0.22$ m and $x_t = 0.075$ m, respectively, as depicted in Figure 2(b). The results for each configuration are shown in Figure 2(c). These results demonstrate that the pressure of the reflected wave, p_r, normalized by the ambient air pressure p_1, increases and the normalized pressure of the transmitted wave, p_t/p_1, decreases monotonically as the number of cylinders increases. The present simulation results are in good agreement with the experimental results by Suzuki *et al.* [42], validating our DEM–CFD scheme for simulating the interaction between shocks and

12

elongated cylindrical objects.

In the second case, to validate the modeling of shock-induced granular dispersion, we simulate the same cases as those in the experiments by Ling *et al.* [13]. The computational setup is also described as Figure 2(a). The shock ($M_a = 1.66$) impacts a 2 mm-thick curtain of 115 μm spherical soda lime particles ($AR = 1$) at an initial volume fraction of 21%. The evolutions of the upstream curtain front (UCF) and downstream curtain fronts (DCF) are tracked in the simulations. As shown in Figure 2(d), the curtain fronts and the rate of curtain expansion obtained from the simulations are in excellent agreement with the experimental measurements. Further, Figure 2(e) shows that the present simulations can accurately reproduce the histories of the transmitted and reflected shock pressures at two monitoring locations of $x_A =$ -0.0686 m and $x_B =$ 0.0641 m.

IV.   RESULTS AND DISCUSSION

Extensive numerical simulations were conducted to examine the propagation of shock waves through randomly packed fiber curtains at Mach number of 1.1, systematically varying fiber aspect ratios ($AR = 1, 2, 4, 8, 12, 16, 20$) or bending flexibility. To balance statistical representativeness with computational feasibility, the total number of particles was carefully controlled: simulations with spherical particles ($AR = 1$) involved with 100,000 particles to ensure statistical resolution, while fiber counts decreased from 40000 ($AR = 2$) to 3390 ($AR = 20$), maintaining a constant solid volume across all cases. The baseline bond bending modulus is set to $E_b = 5 \times 10^8$ Pa, resulting in negligible fiber deformation during dispersal stage for all AR values. Subsequent analyses employed reduced E_b values to systematically evaluate the influence of fiber flexibility.

A.   Fiber dispersion patterns

The temporal evolution of the morphology and extent of shock-induced dispersal of fiber curtains is depicted in Figure 3, which compares four representative cases ($AR = 1, 2, 8, 20$) at $t = 0, 7.8$ and 15 ms. Fibers are colored according to their instantaneous velocity. Full videos visualizing the dynamic dispersal process for each of these representative cases are provided in the supplementary movie 1. At $t = 0$, all configurations exhibit homogeneous
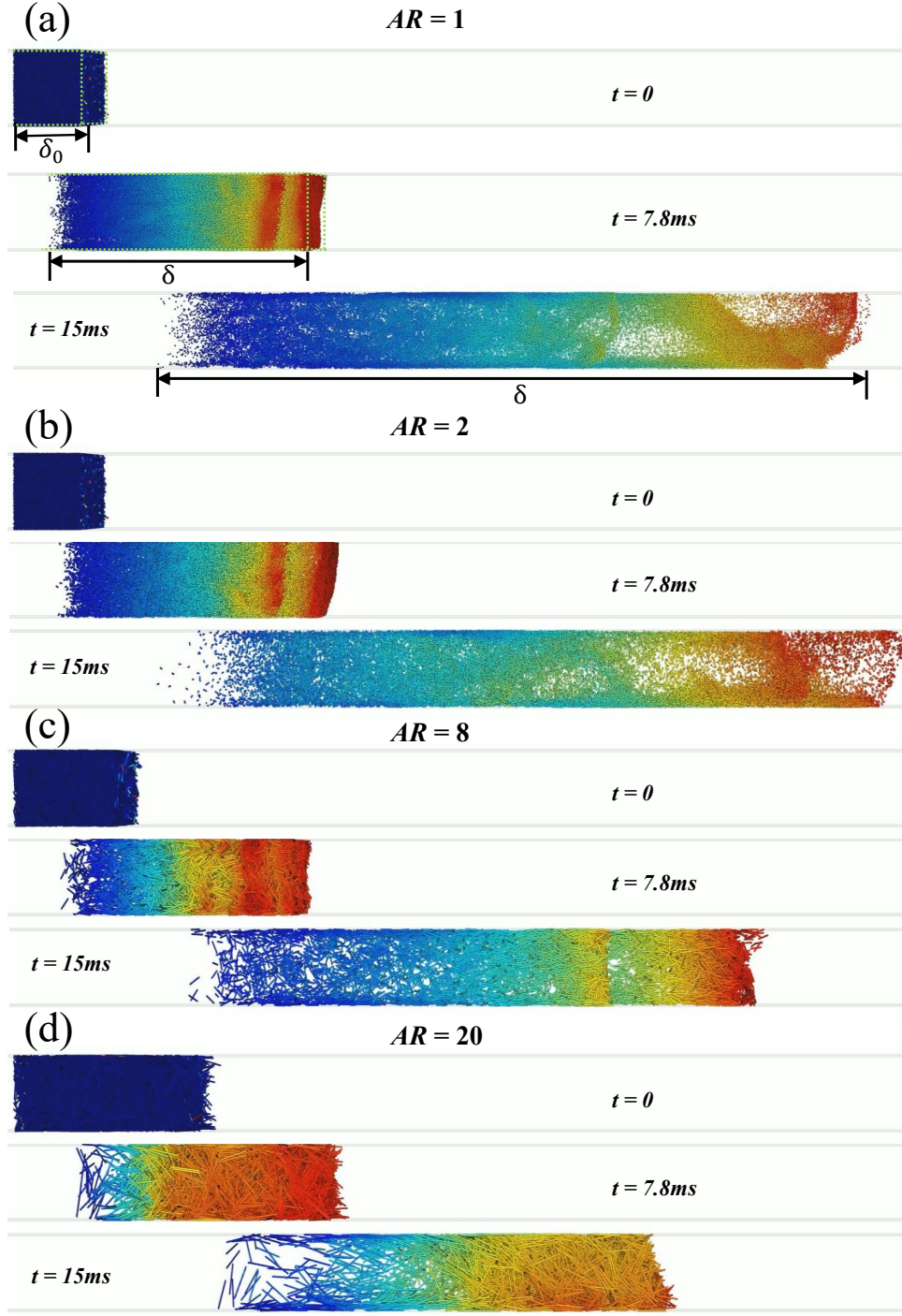
FIG. 3. Snapshots of shock-induced fiber dispersal at $t = 0$, 7.8, and 15 ms for the fiber aspect ratios (a) $AR = 1$, (b) $AR = 2$, (c) $AR = 8$, and (d) $AR = 20$. The color indicates the magnitude of fiber velocity: the velocity increases as the color changes from blue to red. The fibers have a bending modulus of $E_b = 5 \times 10^8$ Pa.

random packing, however, their initial volume fractions ϕ_0 vary significantly due to the excluded volume effect arising from fiber elongation [29]. As detailed in the insert of Figure 4(b), ϕ_0 decreases markedly with increasing AR: spherical particles ($AR = 1$) achieve dense packing with $\phi_0 = 0.58$, while high-AR fibers, such as, $AR = 20$ form considerably sparser fiber beds with $\phi_0 = 0.21$.

Under shock wave loading, all fiber systems, regardless of aspect ratio, exhibit rapid downstream migration accompanied by granular curtain expansion, as illustrated in Figure 3. However, the dispersal characteristics reveal a strong dependence on AR. At $t = 15$ ms, low-AR fiber systems (e.g., $AR = 1$ and 2) display intense non-uniform expansion with significant spatial heterogeneity in fiber distribution. In contrast, high-AR fiber systems (e.g., $AR = 20$) undergo a more restricted expansion. In this case, the observed morphological irregularity arises primarily from the localized migration lag of a limited number of fibers near the rear interface, while the global structural integrity of the dispersing curtain is largely preserved. Figure 4(a) quantitatively depicts the temporal evolution of the normalized curtain length, δ/δ_0, where $\delta(t)$ denotes the instantaneous longitudinal extent of the fiber curtain (measured from front to back edge along the direction of propagation), and δ_0 is its initial value. While all systems show an increase in length, the rate and overall magnitude of expansion differ substantially with AR. For instance, the curtain composed of $AR = 20$ fibers expands to approximately twice its initial length, $2\delta_0$, by $t = 15$ ms, whereas the $AR = 1$ system expands by nearly an order of magnitude, $10\delta_0$, within the same timeframe. Concurrently, Figure 4(b) presents the evolution of the average volume fraction, ϕ, within the dispersing curtain. Intriguingly, this analysis shows that despite the stark initial differences in expansion behavior and extent, the average volume fraction for all systems tends to converge towards a unified decay profile by approximately $t = 10$ ms. This convergence of ϕ despite differing spatial expansion suggests complex internal structural evolutions, which will be explored in the next section.

Figure 5 presents the space-time (x-t) diagrams of the local volume fraction, $\phi_p(x,t)$, for systems with $AR = 1, 2, 8, 12, 16$, and 20, clearly illustrating their distinct dispersal patterns. These diagrams were generated through a discrete layer-wise analysis along the streamwise (x) direction, with the granular curtain partitioned into 2-mm-thick slices. For the low-AR fiber systems ($AR = 1$ and 2), as shown in Figures 5(a) and (b), the dispersal patterns are nearly identical. A defining characteristic is the precipitous drop in volume
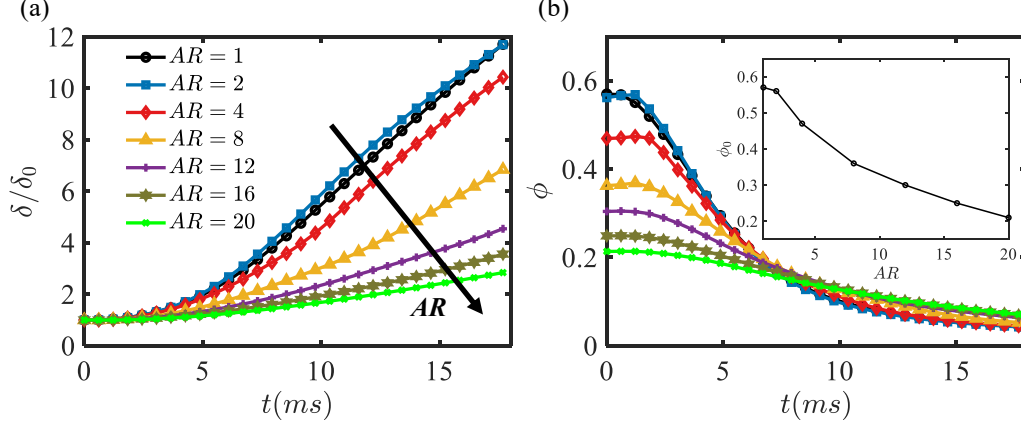
FIG. 4. Dispersal dynamics of the fiber curtains characterized by (a) normalized curtain length δ/δ_0 and (b) average solid volume fraction of the curtain ϕ, in which the inset in (b) shows the dependence of the initial solid volume fraction ϕ_0 on the fiber aspect ratio AR. The fibers have a bending modulus of $E_b = 5 \times 10^8$ Pa.

fraction at the curtain's leading edge around $t \approx 9$ ms. This phenomenon, indicative of a rapid, localized disintegration and accelerated ejection of frontal particles, subsequently leads to this frontal region approaching $\phi_p \approx 0$. Concurrently, a distinct band of higher ϕ_p emerges within the interior of these curtains, signifying the transient formation of internal particle clusters that later dissipate as overall dispersion progresses. Conversely, the high-AR systems (e.g., $AR = 12$, 16, and 20; Figures 5(d)–(f)) exhibit a markedly different behavior. These systems sustain a high ϕ_p at their advancing front throughout the observed period, showing no discernible signs of the frontal disintegration characteristic of their low-AR counterparts. This suggests a significantly more stable and coherent propagation of the leading edge, likely due to enhanced inter-fiber mechanical constraints. The $AR = 8$ system (Figure 5(c)) exhibits a transitional response, displaying characteristics intermediate to the extremes of low and high AR described previously. Although its leading edge eventually experiences a notable decrease in volume fraction, this phenomenon is significantly postponed to approximately $t \approx 14$ ms, indicating a delayed and less intense onset of frontal particle acceleration compared to the $AR = 1$ and 2 systems. Furthermore, the internal particle cluster, identified as a band of high ϕ_p, persists for a longer duration in the $AR = 8$ system than in its lower-AR counterparts, though it does not achieve the same degree of sustained frontal integrity observed in the high-AR systems. These systematically varying,
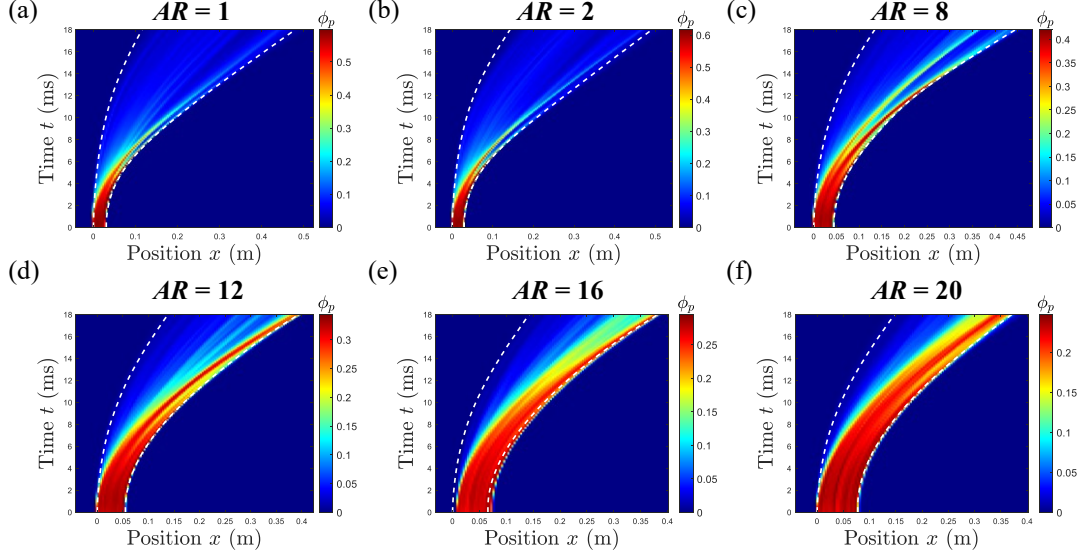
16

FIG. 5. Spatiotemporal x-t diagrams of local solid volume fraction ϕ_p during shock-induced fiber curtain dispersal for the fiber aspect ratios (a) $AR = 1$, (b) $AR = 2$, (c) $AR = 8$, (d) $AR = 12$, (e) $AR = 16$, and (f) $AR = 20$. The fibers have a bending modulus of $E_b = 5 \times 10^8$ Pa. The white dash-lines represent the upstream and downstream air-solid interfaces of the fiber curtains.

AR-dependent dispersal patterns—particularly the differences in the stability of the curtain's leading edge and the persistence of internal clusters—strongly indicate the governing influence of AR-modulated inter-fiber interactions and the resulting structural integrity of the particulate assembly.

The observed variations in dispersal pattern with AR can be primarily attributed to the enhanced effective resistance to curtain expansion, manifesting as an increased effective viscosity or enhanced stability, arising from geometric interlocking in systems of elongated particles. As the AR increases, fiber interlocking becomes more pronounced during dispersal. This facilitates the formation of persistent contact networks that stabilize the fiber curtain, effectively imparting greater structural integrity. Such a mechanism, where interlocking contributes to viscosity-like behavior or augmented static stability, has also been recognized in other granular phenomena, such as mechanical compression [44, 45].

The concept that interlocking enhances effective viscosity and stability is strongly corroborated by the distinct responses of high-AR systems to various macroscopic loads. Figure 6(a) comprehensively illustrates these AR-dependencies by plotting three key parameters, each reflecting a different loading scenario: (i) the angle of repose (characterizing static
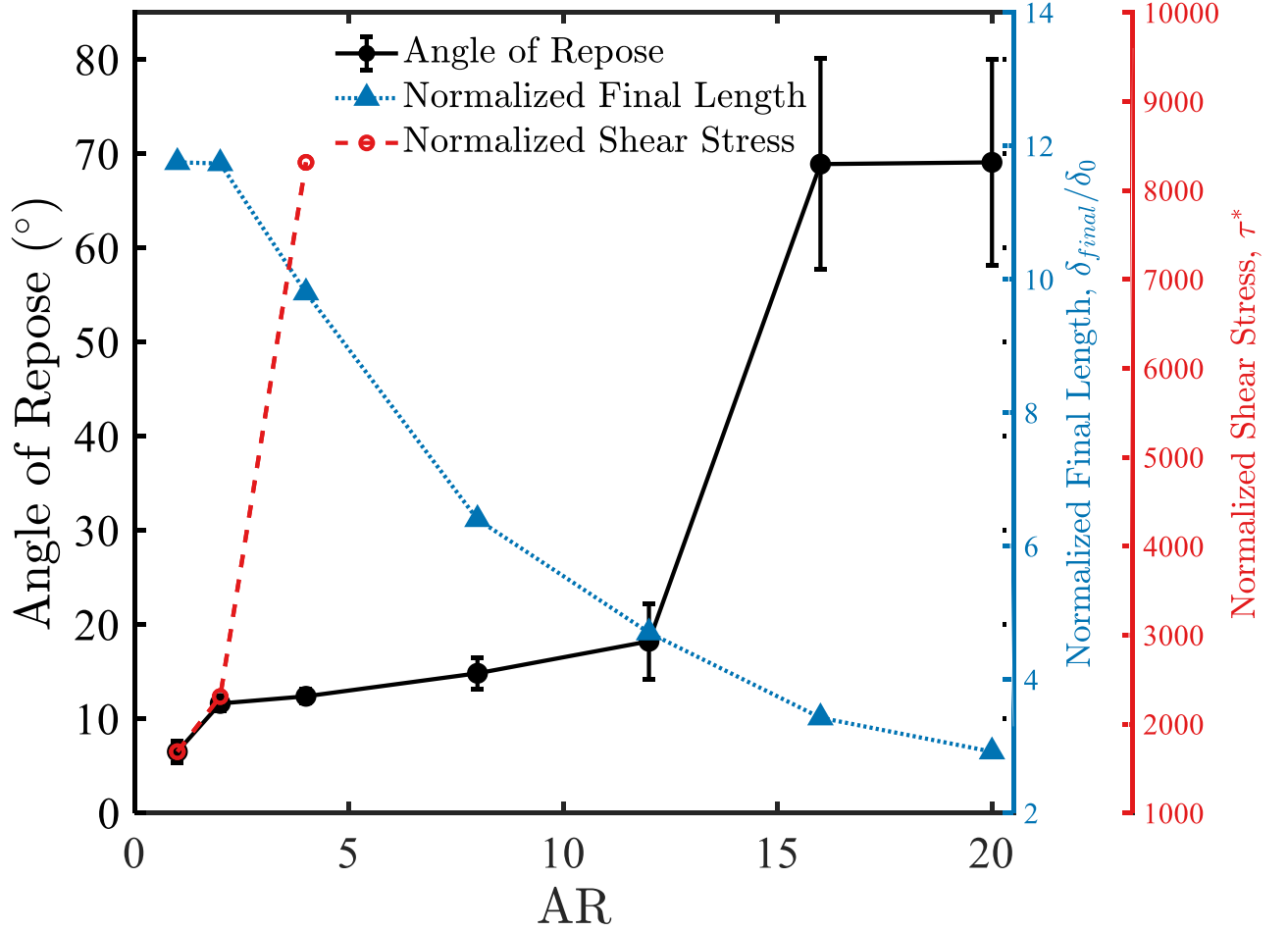
17

FIG. 6. Dependences of the angle of repose, normalized final length of the fiber curtain, and normalized shear stress on the fiber aspect ratio AR.

stability against gravity) is presented against the left y-axis; (ii) the normalized final curtain length, $\delta_{\text{final}}/\delta_0$, (quantifying resistance to shock-induced dispersal) is shown against the primary right y-axis; and (iii) the normalized shear stress, τ^*, from literature (representing effective shear viscosity) is plotted against the secondary right y-axis.

First, focusing on static stability, our simulated angle of repose demonstrably increases with AR, rising from approximately 7° for $AR = 1$ to 70° for $AR = 20$. This quantitative result underscores that high-AR fibers, through superior geometric interlocking, achieve greater static stability. They form significantly more robust and steeper piles that are inherently more resistant to gravitational collapse or minor external perturbations. Next, considering the system's resistance to shock-induced dispersal, the normalized final curtain

length at $t = 18.2$ ms, $\delta_{\text{final}}/\delta_0$, extracted from Figure 4(a), reveals a clear inverse relationship with AR. This directly indicates that systems with stronger geometric interlocking are more effective at resisting the dispersive action of the shock wave, showcasing enhanced stability against dynamic impact. Furthermore, the dynamic resistance to shear deformation also exhibits a pronounced AR-dependence. The normalized shear stress data, τ^*, synthesized from studies on sheared cylindrical particles [46], shows that at a specific solid volume fraction ($\phi = 0.5$), τ^* increases substantially with particle aspect ratio. This heightened impedance to shear flow is principally attributed to the increased difficulty in disentangling and reorienting interlocked elongated particles. This multi-faceted evidence compellingly demonstrates the pivotal role of geometric interlocking in enhancing the effective viscosity and stability of high-AR fiber systems. Such interlocking-driven structural integrity is a central mechanism for understanding their unique dispersal behavior and enhanced stability under shock loading conditions.

To directly examine how geometric interlocking and its associated stabilizing effects materialize at the mesoscale within shocked fiber curtains, we calculated total inter-fiber contact force within each spatial layer by summing all pairwise fiber-fiber interaction forces. The resulting contact force space-time diagrams for two representative systems—$AR = 2$ and $AR = 20$—are shown in Figures 7(a) and 7(b), respectively. Initially, both systems exhibit a rapid accumulation of contact forces during the shock loading phase, indicative of the immediate compressive response of the curtain. However, their subsequent force evolution dynamics diverge significantly, underscoring the role of AR. For the $AR = 2$ system (Figure 7(a)), the enlarged insert reveals that a stress wave propagates through the fiber curtain along transient, densely packed contact chains. This is quickly followed by a complete disintegration of the contact network after approximately $t = 8$ ms as dispersal progresses and inter-fiber contacts are rapidly lost. In contrast, the $AR = 20$ system (Figure 7(b)) demonstrates a markedly different force evolution dynamic. During the initial loading phase, contact forces exhibit a more distributed and comparatively weaker growth, consistent with the damping-like response attributed to an extended network of percolating force chains in long fiber systems [28]. Most importantly, during the subsequent expansion phase, the leading edge of the $AR = 20$ curtain maintains a sustained, high-intensity contact force network. This persistent internal stress provides compelling evidence that geometric interlocking effectively suppresses large-scale instabilities by maintaining the integrity and stability of these critical
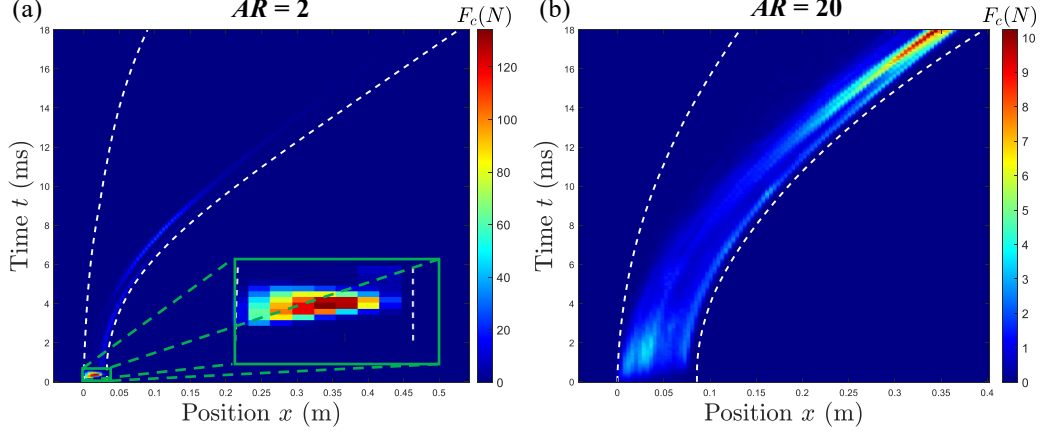
FIG. 7. Spatiotemporal x-t diagrams of mesoscopic contact force F_c for (a) $AR = 2$ (the inset shows the contact force distribution within the curtain at the early stage) and (b) $AR = 20$. The fibers have a bending modulus of $E_b = 5 \times 10^8$ Pa. The white dash-lines represent the upstream and downstream air-solid interfaces of the fiber curtains.

contact networks throughout the dispersal process.

To elucidate how AR-dependent structural characteristics manifest in the kinematic behavior of individual fibers, we analyze the probability density function (PDF) of their streamwise v_x and transverse velocities v_y at $t = 18.2$ ms. For consistency and better comparative clarity, both velocity components are normalized by the post-shock streamwise gas velocity $U_x = 55$ m/s, i.e., we consider v_x/U_x and v_y/U_x. Figure 8(a) presents the PDF of normalized streamwise velocity v_x/U_x. In low-AR systems ($AR < 12$), distribution is broad and nearly uniform in the range $v_x/U_x \in [0.1, 0.82]$, reflecting disordered migration without dominant collective modes. Notably, a small subset of fibers achieves velocities near the upper bound of this range ($v_x/U_x \approx 0.8$), forming a distinct tail in the PDF. These fast-moving fibers, concentrated at the leading edge of the dispersing curtain (as seen in Figure 3), possess significantly higher momentum relative to the bulk, contributing to local instabilities and front interface deformation. In contrast, high-AR systems ($AR > 12$) exhibit a sharply peaked v_x/U_x distribution around 0.5, reflecting a pronounced degree of velocity synchronization and collective migration. This coherent motion arises from robust geometric interlocking among elongated fibers, which fosters the formation of persistent contact networks and stabilizes the curtain's leading-edge morphology. As illustrated in the inset of Figure 8(a), these fiber clusters migrate in a coordinated manner, maintaining structural integrity throughout the
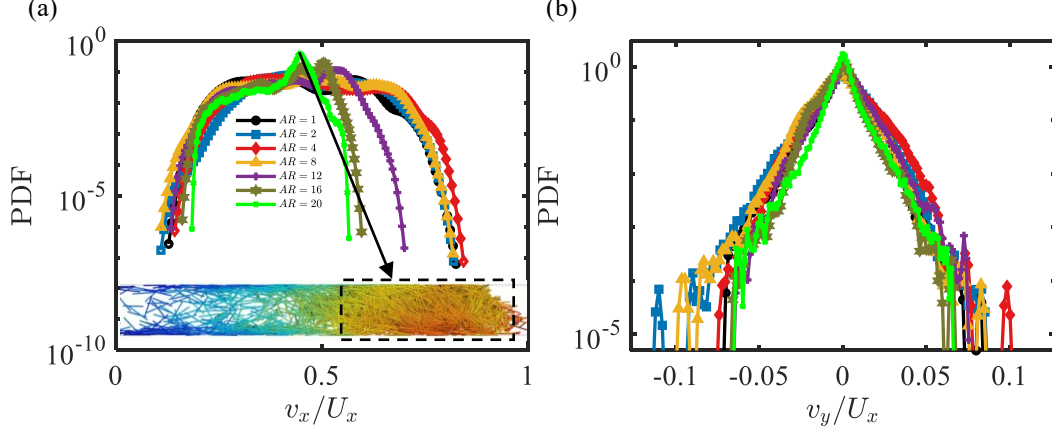
FIG. 8. Probability density functions of the normalized fiber velocity components: (a) v_x/U_x and (b) v_y/U_x at $t = 18.2$ ms. The fibers have a bending modulus of $E_b = 5 \times 10^8$ Pa.

dispersal process. The interplay between these strong clusters and surrounding gas-phase dynamics will be further explored in the following section.

Figure 8(b) presents the PDF of the transverse velocity component, v_y/U_x, across fiber systems of varying aspect ratios. All systems exhibit a distinct peak at $v_y/U_x=0$, consistent with the predominantly axial nature of shock-induced dispersal. However, high-AR systems feature a significantly sharper central peak, indicating a larger fraction of fibers with negligible transverse motion. This constrained lateral mobility is a direct consequence of strong geometric interlocking, which limits out-of-plane movement and reinforces collective alignment. In contrast, low-AR systems display broader v_y/U_x distributions with extended tails, highlighting a non-trivial subset of fibers possessing appreciable transverse velocities. These anomalous lateral excursions disrupt local coherence and are closely associated with the emergence of interfacial instabilities [23] and the onset of non-uniform front morphologies.

B. Cluster-induced resistance

The preceding analysis has revealed that fiber aspect ratio critically influences the stability of the dispersing fiber curtain, leading to the formation of fiber clusters with markedly distinct characteristics. These AR-driven differences in cluster stability and morphology directly govern the resistance imparted by the fiber curtain to the propagating shock wave and subsequent gas flow.
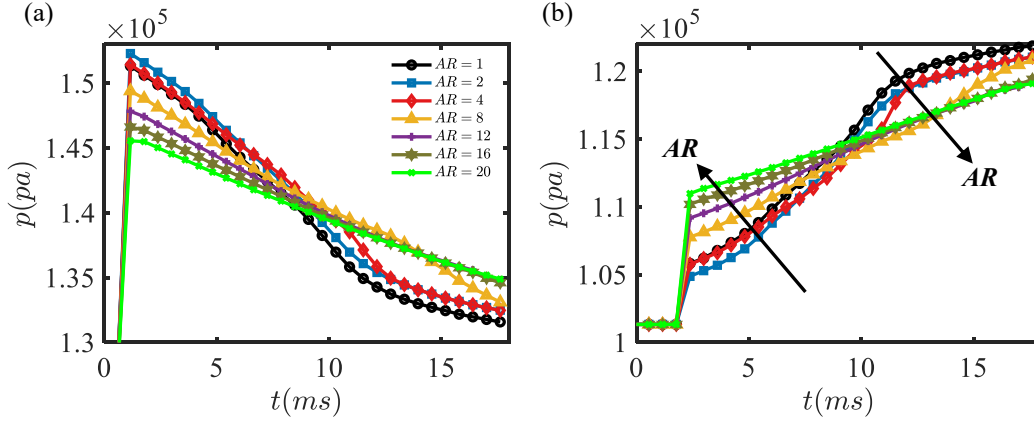
FIG. 9. Time evolution of the pressure p of (a) the reflected wave at Point A and (b) the transmitted wave at Point B for various fiber aspect ratios AR. The fibers have a bending modulus of $E_b = 5 \times 10^8$ Pa.

This cluster-induced resistance is shaped by the interplay of two primary effects tied to these AR-dependent cluster attributes. Firstly, the persistent clusters, which are a manifestation of the enhanced stability in high-AR systems, act as robust porous barriers. These structures significantly impede gas penetration and enhance the overall drag exerted on the curtain. Secondly, the rapid fragmentation of the less stable clusters prevalent in low-AR systems leads to a different mode of interaction. This is characterized by the accelerated dispersal of individual fibers and localized, high-velocity ejections of particles from the dispersing curtain front. While this latter process involves intense local gas-solid momentum exchange, its contribution to the sustained, global resistance of the curtain differs markedly from that of the intact, stable clusters found in high-AR configurations. This section will quantitatively investigate how the AR-dependent dominance and interplay of these two effects, stemming from the varying stability and characteristics of the fiber clusters, collectively determine the temporal evolution and magnitude of the resistance offered by the fiber curtain system.

The quantitative analysis of this cluster-induced resistance commences with an examination of gas-phase dynamics, utilizing pressure and velocity measurements at upstream point A (for reflected wave characteristics) and downstream point B (for transmitted wave characteristics), as depicted in Figures 9 and 10, respectively. The characteristics of the reflected wave at point A (Figures 9(a) and 10(a)) offer a primary insight into the immedi-
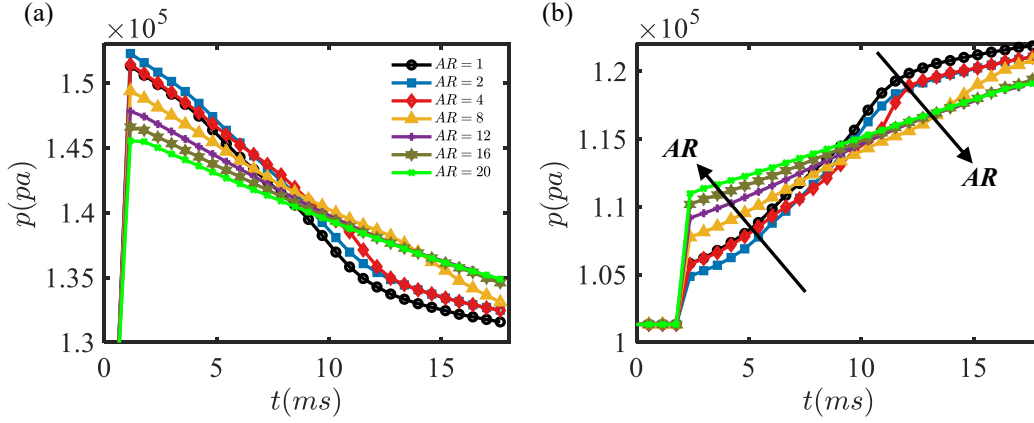
22

FIG. 10. Time evolution of the streamwise air velocity U_x^g of (a) the reflected wave at Point A and (b) the transmitted wave at Point B for various fiber aspect ratios AR. The fibers have a bending modulus of $E_b = 5 \times 10^8$ Pa.

ate attenuation capability of the fiber curtain. A stronger reflected wave inherently signifies a greater portion of the incident shock energy being repelled, and thus a more substantial initial attenuation of the shock by the particulate medium. Our simulations reveal that low-AR systems (e.g., $AR = 1$ to 4), with their higher initial ϕ_0, generate significantly stronger reflected waves (characterized by higher peak pressures and, correspondingly, lower peak upstream gas velocities post-reflection) compared to high-AR systems. This unequivocally demonstrates that a denser initial packing imposes greater immediate shock attenuation effect [47]. The transmitted wave characteristics at point B (Figure 9(b) and 10(b)), representing the shock wave after its interaction with and attenuation by the fiber curtain, further elucidate the AR-dependent resistance, particularly its temporal evolution. Naturally, the presence of a reflected wave implies a reduction in the energy and intensity of the wave transmitted downstream.

All systems exhibit an initial rise in downstream pressure and velocity upon arrival of this attenuated wave, followed by a continued increase during dispersion, the nature of this evolution varies markedly with AR. Initially, systems with higher AR values (which generated weaker reflections) exhibit a stronger and more rapidly rising transmitted wave, reflecting their lower immediate attenuation compared to the denser, low-AR configurations. However, the subsequent evolution reveals more complex dynamics. For low-AR systems, a distinct, highly dynamic phase emerges: the peak rate of pressure growth at point B strikingly coin-

23

cides with the precipitous drop in leading-edge volume fraction and the accelerated ejection of frontal particles (detailed in Figures 5(a) and 5(b) from x-t diagrams). This temporal concurrence signifies a rapid structural collapse of the initial dense packing into a more permeable, rapidly evolving state, which paradoxically facilitates a momentary surge in the downstream pressure accumulation rate, despite their strong initial attenuation. High-AR systems (e.g., $AR = 12$ to 20) transition into a more sustained interaction phase. Here, geometric interlocking stabilizes the leading edge of the fiber curtain, leading to a more modest, near-linear increase in transmitted wave pressure and velocity over an extended duration. This behavior underscores a more persistent, albeit initially less intense, form of resistance and ongoing attenuation.

While the initial overall volume fraction, ϕ_0, offers a first-order explanation for early-stage resistance—evidenced, for instance, by the stronger shock reflection from denser low-AR systems—this static macroscopic parameter inherently fails to capture the dynamic evolution of internal structures and thus becomes insufficient for explaining the sustained differences in behavior observed at later times. Indeed, Figure 5(b) demonstrates that the macroscopic volume fractions across all AR systems eventually converge towards a similarly low level as dispersion progresses. Therefore, a detailed examination from a mesoscopic perspective—one that resolves the formation, evolution, and stability of internal structures such as particle clusters, and their dynamic interaction with the gas phase—is crucial for a complete understanding of the staged nature of the system's response and the underlying mechanisms of cluster-induced resistance.

To characterize these evolving clusters, and link their properties to the observed resistance, we define a cluster as a contiguous region where the local fiber volume fraction, $\phi_p(x, t)$, exceeds a threshold of $0.6\phi_0$. This threshold was empirically determined to best capture coherent, densely-packed regions that visually corresponded to mechanically significant agglomerations, while filtering out more tenuous, transient fiber groupings. Fibers within these regions are thus identified as constituting a cluster. Figure 11 visually demonstrates the morphology and evolution of these defined clusters, highlighted in green, presenting snapshots for representative $AR = 2$ and $AR = 20$ systems at $t = 7.8$ ms and $t = 15$ ms. At $t = 7.8$ ms, distinct differences in cluster morphology are already apparent. For the $AR = 2$ system (Figure 11(a)), rapid dispersal and expansion have led to a significantly reduced overall cluster presence. The remaining clustered fibers are primarily concentrated in a band
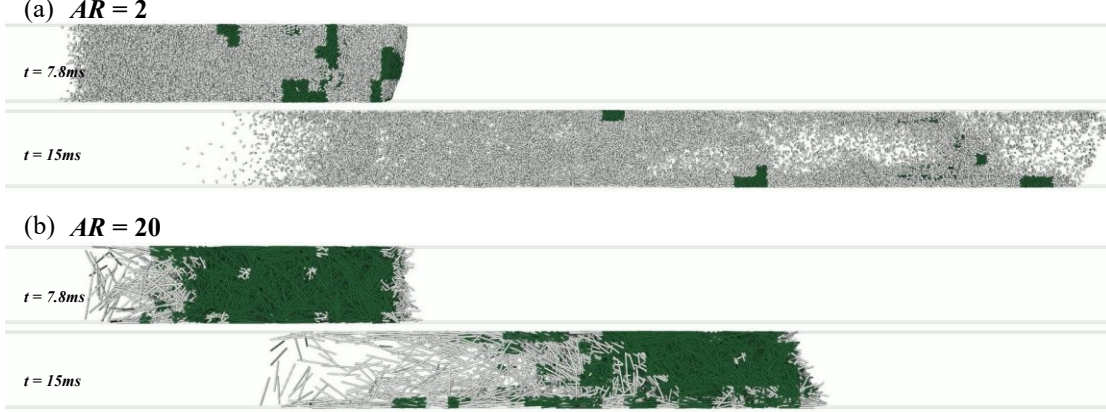
FIG. 11. Snapshots of the evolution of the fiber clusters (highlighted in green) for the low-AR ($AR = 2$) and high-AR ($AR=20$) systems at $t = 7.8$ ms and $t = 15$ ms. The fibers have a bending modulus of $E_b = 5 \times 10^8$ Pa.

within the curtain's interior and at the leading edge. Notably, as observed from the overall dispersal dynamics as show in Figure 3, fibers within these clusters tend to possess high velocities, suggesting strong localized acceleration mechanisms that will be explored further in the context of pressure gradient analysis. Alternatively, the $AR = 20$ system (Figure 11(b)) at the same time instance, benefiting from enhanced inter-fiber interlocking, shows that the vast majority of fibers still participate in forming a large, relatively coherent cluster structure. These disparities become even more pronounced at $t = 15$ ms. In the $AR = 2$ system (Figure 11(a)), only a few isolated remnants of clustered fibers can be identified, indicating near-complete fragmentation. Yet, the $AR = 20$ system (Figure 11(b)) continues to exhibit substantial, large-scale clusters, particularly at its stabilized leading edge, underscoring the persistent nature of these structures due to enhanced geometric interlocking.

To quantify these visually observed differences in cluster evolution, two key parameters are extracted from the identified clusters, with their temporal evolution depicted in Figure 12: the average cluster volume fraction, $\bar{\phi}_c$, representing the internal packing density of the clusters, and the cluster volume ratio, η, defined as the ratio of the volume of the fibers within these identified clusters $V_{cluster}$ to the total volume of all the fibers in the system V_{total}: $\eta = V_{cluster}/V_{total}$. Analysis of $\bar{\phi}_c$ in Figure 12(a) reveals that, on average, clusters formed by higher AR fibers are inherently less dense, reflecting the looser packing achievable by longer fibers even within these agglomerated structures. This trend is consistent with
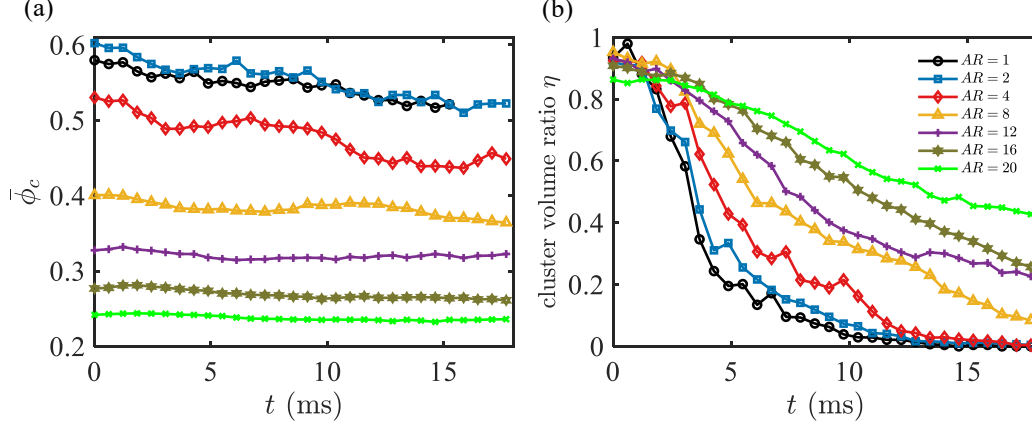
FIG. 12. Time evolution of the (a) average solid volume fraction in the clusters $\bar{\phi}_c$ and (b) cluster volume ratio η for the fiber curtains with various fiber aspect ratios AR. The fibers have a bending modulus of $E_b = 5 \times 10^8$ Pa.

the initial ϕ_0. The evolution of η (Figure 12(b)) shows that in the initial stage of dispersal, nearly all fiber volume across all AR values is contained within a single, large, identifiable cluster, resulting in η approaching 1. As dispersal progresses, η diminishes for all ARs. However, a crucial distinction emerges: high-AR systems (e.g., $AR = 12$ to 20) maintain a substantially higher η, retaining approximately 40% of their fiber volume within identifiable clusters at later times, whereas clusters in the $AR = 1$ system almost completely disintegrate ($\eta \to 0$).

The role of these evolving clusters in dictating gas flow resistance is further elucidated by the pressure gradient (∇p) x-t diagram presented in Figure 13. These pressure gradients consistently remain negative within the curtain region, reflecting higher upstream pressure compared to downstream. Moreover, the magnitudes of these adverse pressure gradients are significantly more pronounced at the locations of dense clusters, as visually corroborated by comparing with the cluster indicators in Figure 5.

In the initial stages, $AR = 1$ and 2 systems, with their higher $\bar{\phi}_c$ values, exhibit the largest pressure gradient magnitudes. This strong initial gradient vigorously drives local particle motion, leading to the high fiber velocities observed within these early-formed clusters in low-AR systems. While this might initially contribute to some local cluster compaction, the sustained intense acceleration in these less interlocked systems ultimately causes leading-edge particle velocities to significantly exceed the mean. This, as previously discussed, triggers
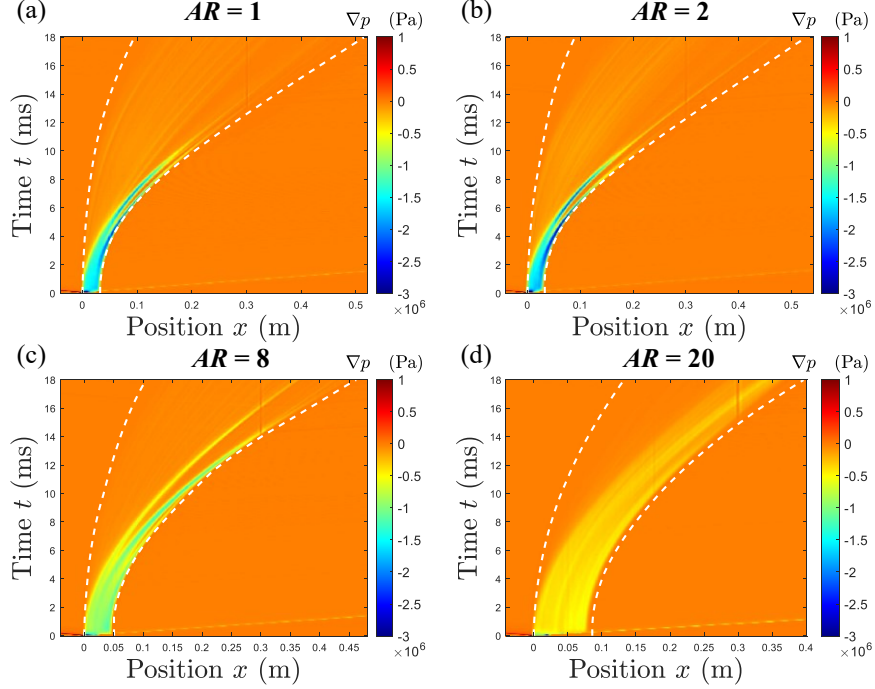
26

FIG. 13. Spatiotemporal x-t diagrams of the pressure gradient in shock-induced fiber curtain dispersal for the fiber aspect ratios of (a) $AR = 1$, (b) $AR = 2$, (c) $AR = 8$, and (d) $AR = 20$. The white dash-lines represent the upstream and downstream air-solid interfaces of the fiber curtains. The fibers have a bending modulus of $E_b = 5 \times 10^8$ Pa.

interfacial instabilities and accelerates the overall dispersal of the fiber curtain, thereby diminishing their capacity for long-term gas flow resistance (consistent with the later-stage transmitted wave behavior in Figures 9(b) and 9(b)). Conversely, in high-AR systems (e.g., $AR = 20$), the inherently lower $\bar{\phi}_c$ results in a weaker but notably more persistent pressure gradient across their stable, interlocked cluster structures. This sustained, albeit more modest, adverse pressure gradient enables the leading-edge clusters to continuously impede gas flow over a protracted period. This translates into a more effective sustained resistance to the flow, particularly at later times, underscoring the importance of long-term cluster integrity, facilitated by geometric interlocking, for achieving superior overall shock attenuation in these high-AR configurations.
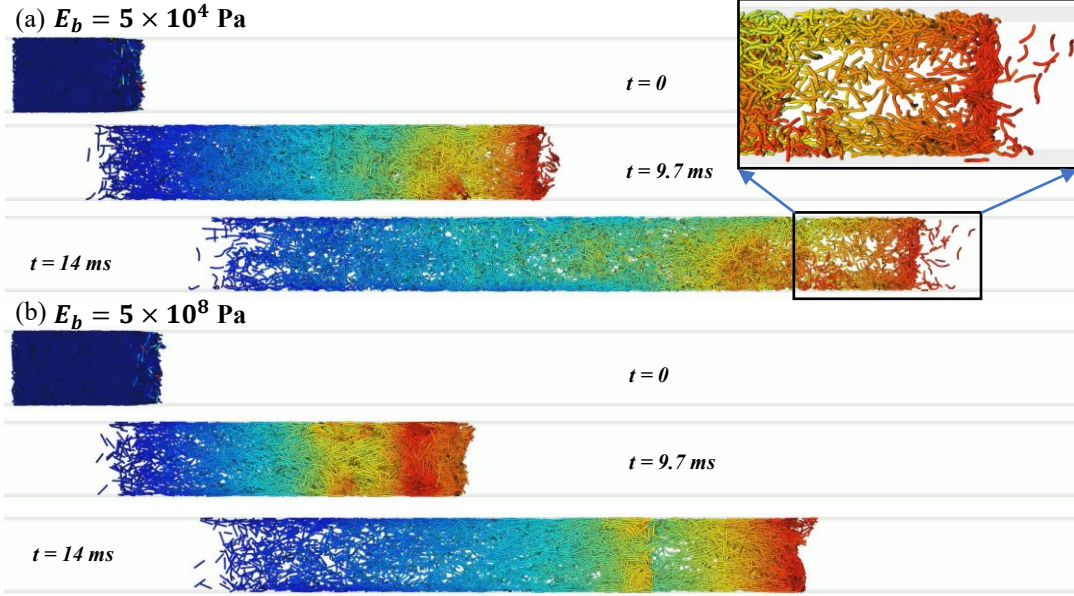
FIG. 14. Time-sequential snapshots of the fiber dispersals at the time instants $t = 0$, 9.7 ms, and 14 ms for the fiber bending moduli of (a) $E_b = 5 \times 10^4$ Pa and (b) $E_b = 5 \times 10^8$ Pa. The color indicates the magnitude of fiber velocity: the velocity increases as the color changes from blue to red. The fibers have an aspect ratio of $AR = 8$.

C. Effect of fiber flexibility

Significant fiber bending deformation occurs for the very flexible fibers subject to the shock impact. Increased fiber flexibility, corresponding to a reduced fiber bending modulus E_b (defined in Eqs. (3)-(6)), leads to more pronounced fiber bending deformation due to the air-fiber interaction and fiber-fiber contacts. To explore the effect of fiber flexibility on the shock-driven fiber dispersion, numerical simulations are performed to analyze the systems with a fixed fiber aspect ratio of $AR = 8$ and different bending moduli E_b varying in a wide range of between 5×10^4 Pa and 5×10^8 Pa, which enables a comprehensive evaluation of how the fiber bending deformation at various degrees influences air-solid interactions, fiber dynamics, and air flows.

Figure 14 shows time-sequential snapshots of the fiber dispersals for the highly flexible fibers with $E_b = 5 \times 10^4$ Pa and relatively stiff fibers with $E_b = 5 \times 10^8$ Pa. The stiff fibers tend to maintain a more coherent, albeit expanding, structure (Figure 14(b)), while the highly flexible fibers (Figure 14(a)) exhibit more irregular and diffusive morphology, in which more
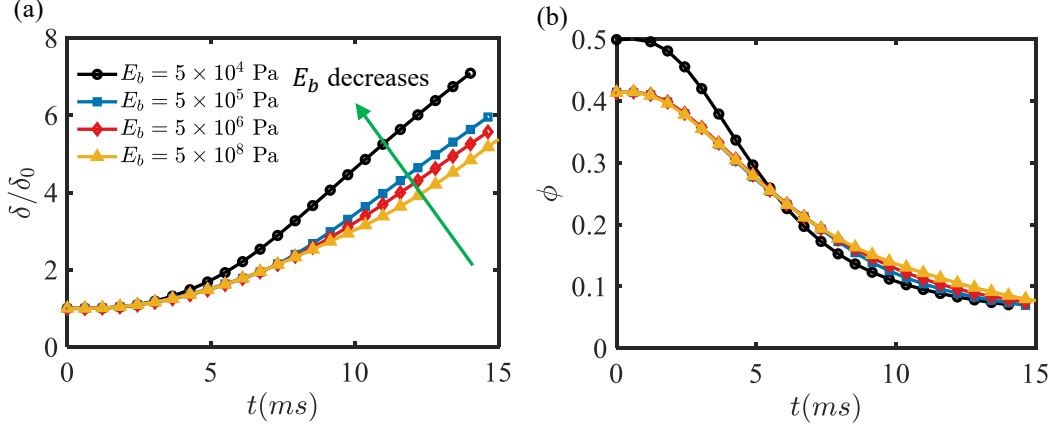
FIG. 15. Time evolutions of the (a) normalized curtain length δ/δ_0 and (b) average solid volume fraction ϕ for the fiber curtains with various fiber flexibilities characterized by the fiber bending modulus E_b. The fibers have an aspect ratio of $AR = 8$.

pronounced individual fiber deformation is observed. The leading edge of the highly flexible fiber curtain is characterized by some scattering particle ejections at $t = 9.7$ and 14 ms, indicating that the interlocking is weaker and the motion of the fibers is less constrained as the fibers become more flexible. Comparing Figures 14(a) and 14(b), the leading edge of the highly flexible fibers travels further than that of the stiff fibers at a specified time instant (e.g. $t = 9.7$ ms or 14 ms), resulting a greater expansion of the curtain. The time evolution of the normalized length of the fiber curtain δ/δ_0 for various fiber bending moduli E_b is shown in Figure 15(a). It is observed that the curtain length generally increases faster as the fiber flexibility increases (i.e. E_b decreases), and more significant increase in δ/δ_0 is obtained by decreasing E_b from 5×10^5 Pa to 5×10^4 Pa. This faster expansion of the more flexible fiber curtain attributes to the weaker interlocking and the particle ejections in the leading edge. In addition, as shown in Figure 15(b), the highly flexible fibers with $E_b = 5 \times 10^4$ Pa are packed more densely with a large solid volume fraction of $\phi = 0.5$ at the onset of the shock impact ($t = 0$), due to the significant fiber deformation. Thus, at the early stage of the dispersion ($t < 5$ ms), the highly flexible fibers gain larger accelerations due to the larger air drag forces exerted on the fibers, which are caused by the larger ϕ (corresponding to the poor permeability of the fiber curtain). This initial large acceleration also contributes to the fast expansion of the highly flexible fiber curtain.

It is interesting to note that the dispersal behaviors of the highly flexible fibers, as illus-
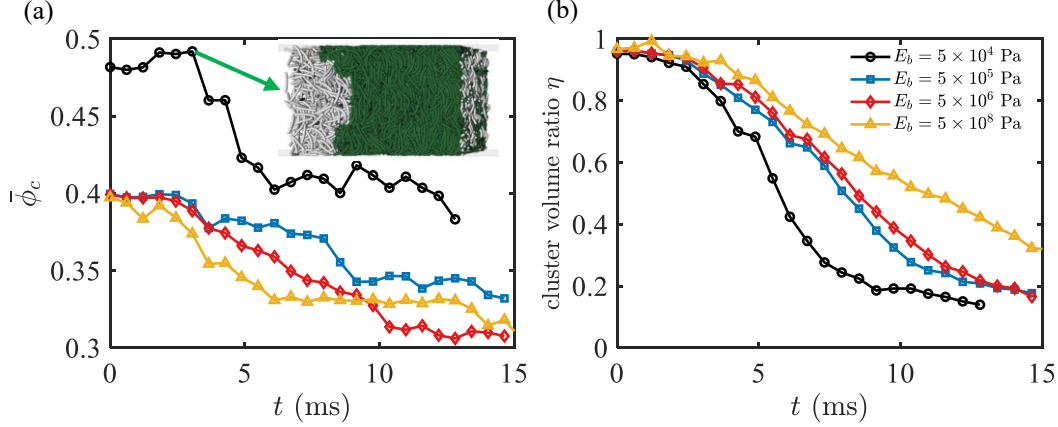
FIG. 16. Time evolutions of the (a) average solid volume fraction in the clusters $\bar{\phi}_c$ and (b) cluster volume ratio η for the fiber curtains with various fiber bending moduli E_b. In the insert of (a), the green fibers belong to the clusters. The fibers have an aspect ratio of $AR = 8$.

trated in Figures 14 and 15, are similar to those of the low-AR fibers, as shown in Figures 3 and 4. Therefore, the effects of increasing fiber flexibility are analogous to those of decreasing fiber aspect ratio.

The fiber flexibility has an impact on the properties of the clusters which evolve during the dispersion. As shown in Figure 16(a), the clusters of the more flexible fibers are generally packed more densely with larger average solid volume fractions $\bar{\phi}_c$. For the highly flexible fibers with $E_b = 5 \times 10^4$ Pa, the clusters are compacted by the shock with increasing $\bar{\phi}_c$ over time at the early stage ($t < 4$ ms), and a large cluster (represented by the green fibers in the insert in Figure 16(a)) is formed on the leading side of the curtain. The fibers exhibit significant bending deformation in the densified cluster. After reaching the peak at $t = 4$ ms, $\bar{\phi}_c$ experiences a sharp decline, which corresponds to the rapid expansion of the clusters driven by the shock. The cluster volume ratio η, defined as the ratio of the volume of the fibers in the clusters to the total volume of all the fibers in the system, decreases much faster with time for $E_b = 5 \times 10^4$ Pa, as shown in Figure 16(b), indicating that the clusters of the highly flexible fibers, which possess lower shear strengths, have shorter life spans.

Figures 17(a) and 17(b) show the spatiotemporal x-t diagrams of local solid volume fraction ϕ_p and air pressure gradient ∇p, respectively, for the highly flexible fibers with $E_b = 5 \times 10^4$ Pa, which are similar to the corresponding diagrams for the stiff fibers with $E_b = 5 \times 10^8$ Pa in terms of the distribution patterns. Nevertheless, the greater peak ϕ_p is
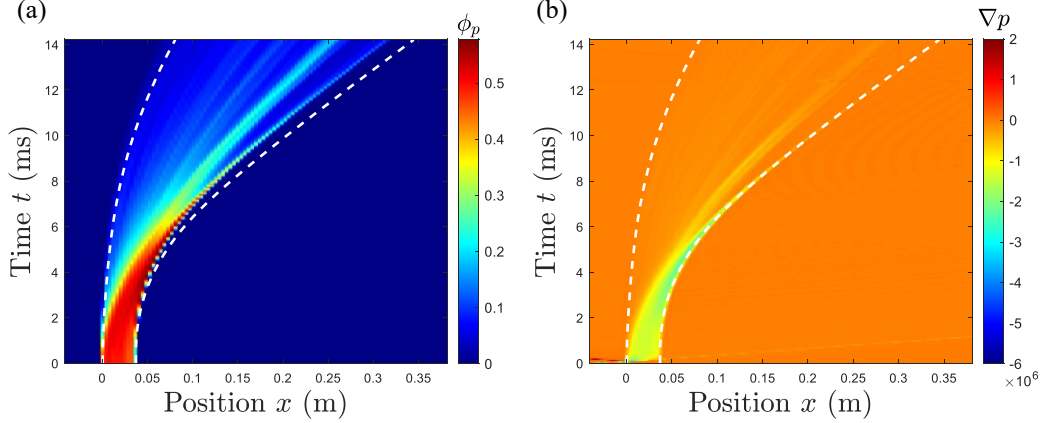
30

FIG. 17. Spatiotemporal x-t diagrams of (a) local solid volume fraction ϕ_p and (b) air pressure gradient ∇p for the highly flexible fibers with $E_b = 5 \times 10^4$ Pa under the shock loading. The fibers have an aspect ratio of $AR = 8$. The white dash-lines represent the upstream and downstream air-solid interfaces of the fiber curtains.

obtained for $E_b = 5 \times 10^4$ Pa compared to $E_b = 5 \times 10^8$ Pa, consistent with the results in Figure 16(a). At the early stage ($t < 4$ ms), due to the formation of the denser clusters with the highly flexible fibers, the negative air pressure gradients of larger magnitudes are induced on the leading side of the curtain, and the negative pressure gradients are sufficiently strong to eject some fibers forward away from the front of the moving curtain (Figure 14(a)).

According to the results in this section, the fiber flexibility has impacts on the packing density and rate of reduction (quantified by $d\eta/dt$) of the clusters, by which the expansion of the curtain and fiber ejection are influenced.

D. Scaling law for expansion of a dense flexible fiber curtain

Elucidating the dynamic expansion of a dense flexible fiber curtain under the shock wave impact is vital for applications like shock mitigation and advanced compressible multiphase flow modeling. Based on the present simulation results, a scaling law for the time-dependent length of the fiber curtain $\delta(t)/\delta_0$ is obtained for the fibers with various aspect ratios AR and flexibility.

Variation in fiber aspect ratio AR naturally induces difference in the initial solid volume fraction ϕ_0, due to distinct shape-dependent packing characteristics. Thus, the scaling law

31

should explicitly include ϕ_0.

To describe the dynamic expansion of the curtains of spherical particles hit by a shock, DeMauro *et al.* [20] derived a scaling correlation of the curtain length of the spherical particles at various solid volume fractions. The derivation begins from a force balance equating the curtain's inertial response to the aerodynamic drag exerted by the shock wave,

$$\phi_0 \rho_f A \delta_0 \frac{d^2 x}{dt^2} = \frac{1}{2} C_D \rho_{ind} \left(U_{ind} - \frac{dx}{dt} \right)^2 A, \tag{21}$$

where $\phi_0 \rho_f A \delta_0$ represents the effective mass of the particle curtain, $\frac{d^2 x}{dt^2}$ represents the effective acceleration of the curtain's center of mass, treated as a bulk object under shock loading, and the right-hand side is the aerodynamic drag, where C_D is the drag coefficient, ρ_{ind} the induced gas density, and $u_{ind} - \frac{dx}{dt}$ is the relative velocity between gas and fiber curtains. Assuming early-stage dynamics where $\frac{dx}{dt} \ll U_{ind}$, and approximating $\rho_{ind} \approx \rho_1$ (the pre-shock ambient gas density), Eq. (21) simplifies to:

$$\phi_0 \rho_f A \delta_0 \frac{d^2 x}{dt^2} \approx \frac{1}{2} C_D \rho_1 U_{ind}^2 A. \tag{22}$$

The integration of the above equation yields,

$$x(t) = \frac{1}{4} C_D \frac{\rho_1}{\phi_0 \rho_f \delta_0} \left(U_{ind} t \right)^2. \tag{23}$$

Assuming the curtain length $\delta(t)$ increases linearly with $x(t)$ by a factor of κ,

$$\delta(t) = \delta_0 + \kappa x(t), \tag{24}$$

Substituting Eq.(23) into Eq. (24) gives,

$$\delta(t)/\delta_0 = 1 + \frac{\kappa}{4} C_D \frac{\rho_1}{\phi_0 \rho_f} \left(\frac{U_{ind} t}{\delta_0} \right)^2. \tag{25}$$

As discussed in [20], the drag coefficient C_D scales with the solid volume fraction ϕ_0 in the form,

$$C_D \propto \phi_0^{3/2} / \left(1 - \phi_0 \right)^2 \tag{26}$$

Substituting Eq. (26) into Eq. (25), a scaling law of the curtain length can be obtained as,

$$\frac{\delta(t)}{\delta_0} - 1 \propto \left[\frac{\phi_0^{1/4} U_{ind} t}{\left(1 - \phi_0 \right) \delta_0} \right]^2 \tag{27}$$
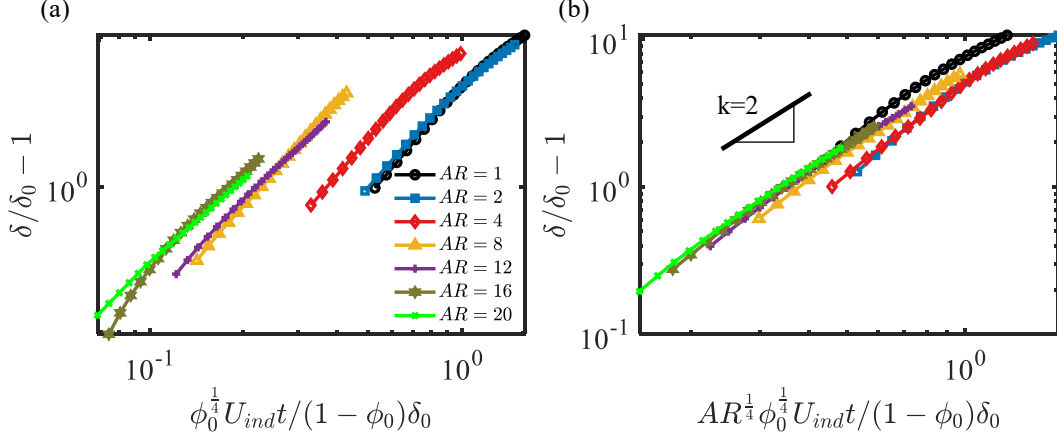
32

FIG. 18. Scaling laws for spreading of flexible fiber curtains with different aspect ratios: (a) incorporation ϕ_0, (b) incorporation ϕ_0 and AR. The fibers have a bending modulus of $E_b = 5 \times 10^8$ Pa.

The scaling represented by Eq. (27) works well for the spherical particle curtains with various solid volume fractions ϕ_0 [20]. Nevertheless, as shown in Figure 18(a), the data deviate more from those of the spherical particles ($AR = 1$) as the fiber aspect ratio AR increases. Thus, the fiber elongation should be considered in the scaling law. The particle aspect ratio AR has an impact on the drag force, and the modified drag coefficient C_D is assumed to follow,

$$C_D \propto \frac{\phi_0^{3/2}}{(1 - \phi_0)^2} \cdot AR^m, \tag{28}$$

where the exponent of $m = 1/2$ was obtained by best fitting to the simulation data. Consequently, a scaling law can be determined for the fiber curtains considering the effect of the fiber aspect ratio AR,

$$\frac{\delta(t)}{\delta_0} - 1 \propto \left[\frac{AR^{1/4} \phi_0^{1/4} U_{ind} t}{(1 - \phi_0) \delta_0} \right]^2. \tag{29}$$

As shown in Figure 18(b), the data tend to collapse, but certain deviations exist. In the correlation of Eq. (29), the effect of AR on the drag force is considered, while the impacts of AR on the fiber-fiber contacts and cluster properties are neglected, which may cause the data deviations in Figure 18(b).

To assess the influence of fiber flexibility on the dispersal dynamics, the results with identical fiber aspect ratio of $AR = 8$ but different fiber flexibilities, characterized by the fiber bending modulus E_b, are analyzed. As shown in Figure 19(a), the dispersal data of the
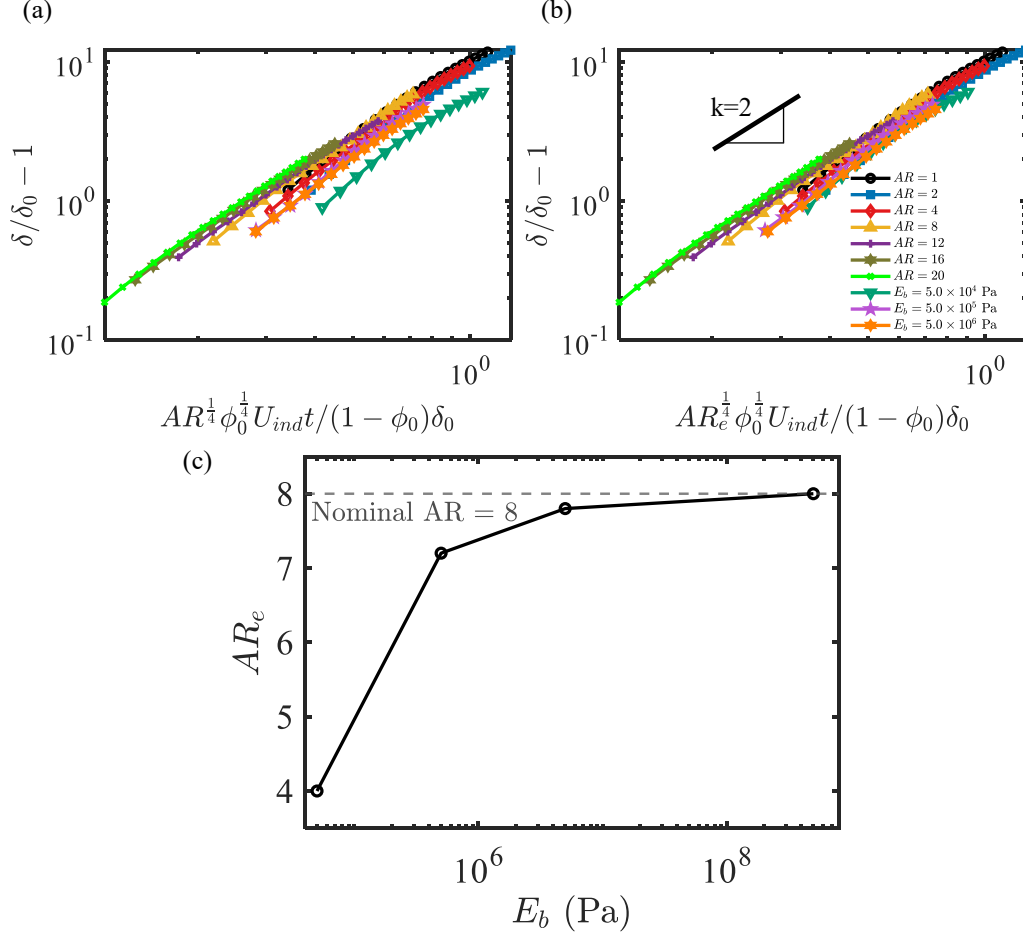
33

FIG. 19. Effect of fiber flexibility on the scaling correlation of the expansion of the fiber curtains: (a) scaling with the fiber aspect ratio AR, (b) improved collapse with the effective aspect ratio AR_e, and (c) variation of AR_e with fiber bending modulus E_b.

highly flexible fibers with a smaller modulus of $E_b = 5.0 \times 10^4$ Pa deviate markedly below the master curve of the more rigid fibers with $E_b = 5.0 \times 10^8$ Pa, underscoring that the significant fiber deformation increase the curtain expansion. Under the shock loading, less interlocking and reduced gas-fiber drag forces are obtained for the more flexible fibers that experience larger bending deformations.

To account for the effects of the fiber deformation on the packing density, an effective aspect ratio AR_e was introduced by [48]. A gyration tensor $\boldsymbol{S}$ [49] was defined as,

$$S_{mn} = \frac{1}{N} \sum_{i=0}^{N-1} (r_m^i - r_m^{cm})(r_n^i - r_n^{cm}), \tag{30}$$

where N was the total number of spherical nodes used to discretize a fiber, vector $\boldsymbol{r}^i$ denoted

34

the position of the i-th node, and vector $\boldsymbol{r}^{cm}$ was the position of the center of mass of the fiber. Three eigenvalues of this gyration tensor were determined as λ_1, λ_2, and λ_3, which followed $\lambda_1 \geq \lambda_2 \geq \lambda_3$. An effective aspect ratio of a fiber AR_e could be calculated by

$$AR_e = \sqrt{\frac{\lambda_1}{max\left[\lambda_3, d_f^2/12\right]}}, \tag{31}$$

in which d_f was the diameter of the fiber and $max[-]$ function returned the larger value between λ_3 and $d_f^2/12$. According to the previous work [48], the fibers of different flexibilities but the same effective aspect ratios AR_e had almost the same packing density.

In this work, the ensemble-averaged effective aspect ratios AR_e are computed for the dispersal processes with the fibers of various flexibilities. The dependence of AR_e on the fiber bending modulus E_b is shown in Figure 19(c), in which the effective fiber aspect ratio AR_e approaches the nominal or real AR as E_b increases. Using the effective aspect ratio AR_e to replace the real aspect AR in Eq. (29), the modified scaling law is obtained as

$$\frac{\delta(t)}{\delta_0} - 1 \propto \left[\frac{AR_e^{1/4}\phi_0^{1/4}U_{ind}t}{(1-\phi_0)\delta_0}\right]^2. \tag{32}$$

Based on this scaling, as shown in Figure 19(b), the fiber curtain expansion data tend to collapse for the fibers with various flexibilities and aspect ratios. This unified collapse highlights the pivotal roles of fiber shape and flexibility in shock-driven spreading dynamics, and provides a predictive tool for the expansion of the flexible fiber curtains.

V. CONCLUSIONS

An investigation in the shock-induced dispersal of dense flexible fiber curtains is presented in this study, and the critical roles of fiber aspect ratio AR and flexibility in the granular dispersal patterns and shock wave attenuation are elucidated. Based on the three-dimensional (3D) simulation results using a coupled DEM-CFD approach, we demonstrate that AR fundamentally determines the dispersal characteristics. Low-AR fiber systems undergo rapid, heterogeneous expansion with pronounced particle ejections. In contrast, high-AR systems leverage the geometric interlocking to form persistent and shear-resistant clusters that effectively suppress the particle ejections and significantly bolster the shock attenuation over time.

The mechanisms underpinning cluster-induced resistance to the shock propagation are found to stem from a complex interplay between the shear yield strengths and the evolving solid volume fractions of the clusters. The initial shock impact consolidates the fiber curtain into a large cluster for all the fiber types. Compared to the high-AR fiber systems, the low-AR fiber systems exhibit stronger resistance to the shock propagation at the early stage due to their denser packings with larger solid volume fractions, causing larger magnitudes of air pressure gradients through the curtain. However, after a period of the wave propagation, clusters formed by the low-AR fibers rapidly disintegrate and simultaneously strong fiber ejections occur, leading to weakened resistance to the shock waves at the late stage. In contrast, high-AR systems exhibit weaker resistance to the shock at the early stage due to their lower solid volume fractions. The clusters of the high-AR fibers have larger shear strengths due to the geometric interlocking, and therefore they can survive and maintain strong resistance to the shock for longer time duration. In conclusion, the low-AR and high-AR fibers have different two-stage characteristics of the shock resistance, due to the differences in the cluster properties for the two types of fibers.

Fiber flexibility, quantified by the fiber bending modulus E_b, determines the fiber bending deformation due to air-fiber interaction and fiber-fiber contacts. Compared to the stiff fibers, at the early stage, more flexible fibers with smaller E_b are compacted to form denser clusters with larger fiber bending deformation, and these denser clusters are reduced faster, manifested by the sharp decrease in cluster volume ratio η, due to the weaker interlocking and lower shear strengths of the highly flexible fiber clusters. Attributed to the easy escape of the individual fibers from the clusters, more rapid expansion with significant fiber ejections on the leading side is obtained for the highly flexible fiber curtains. It is noted that the effects of increasing fiber flexibility on the fiber dispersals are analogous to those of decreasing fiber aspect ratio, as both lead to weakened clusters.

Finally, a generalized scaling law is proposed to describe the dynamic evolution of the length of the fiber curtains. The fiber aspect ratio AR should be included in the scaling correlation to account for the effect of fiber elongation on the air drag. Further, an effective fiber aspect ratio AR_e, which decreases as the fiber experiences larger bending deformation, is introduced to replace the real fiber aspect ratio AR to account for the effect of fiber flexibility on the air-fiber interaction. The present findings provide some updated understandings of dispersal mechanics of the flexible fibers impacted by an air shock, which give some

implications for the use of fibrous materials to achieve the shock attenuation.

---

[1] A. Neri, T. Esposti Ongaro, G. Macedonio, and D. Gidaspow, Multiparticle simulation of collapsing volcanic columns and pyroclastic flow, Journal of Geophysical Research: Solid Earth **108** (2003).

[2] J. Dufek, The fluid mechanics of pyroclastic density currents, Annual Review of Fluid Mechanics **48**, 459 (2016).

[3] A. Britan, H. Shapiro, and G. Ben-Dor, The contribution of shock tubes to simplified analysis of gas filtration through granular media, Journal of Fluid Mechanics **586**, 147 (2007).

[4] J. O'Donovan, E. Ibraim, C. O'Sullivan, S. Hamlin, D. Muir Wood, and G. Marketos, Micromechanics of seismic wave propagation in granular materials, Granular Matter **18**, 1 (2016).

[5] J. Bakken, T. Slungaard, T. Engebretsen, and S. O. Christensen, Attenuation of shock waves by granular filters, Shock Waves **13**, 33 (2003).

[6] A. Kumar and V. Pathak, Shock wave mitigation using zig-zag structures and cylindrical obstructions, Defence Technology **17**, 1840 (2021).

[7] M. Fakourihassanabadi, B. Guerreiro, J. Gaudet, M. H. Martin, S. Abbasi, S. Thorpe, and D. Guay, Fabrication of a Ti-based 3D porous transport layer for PEMWEs using ShockWave-induced spraying and cold spray, Surface and Coatings Technology **477**, 130353 (2024).

[8] D. Ran, J. Cheng, R. Zhang, Y. Wang, and Y. Wu, Damages of underground facilities in coal mines due to gas explosion shock waves: an overview, Shock and Vibration **2021**, 8451241 (2021).

[9] J. Capecelatro and J. L. Wagner, Gas–particle dynamics in high-speed flows, Annual Review of Fluid Mechanics **56**, 379 (2024).

[10] Z. Z. Yu, Y. Ren, Y. Shen, J. Y. Lin, and H. Ding, Evolution of particle cloud after being

impacted by a planar shock: Particle-resolved simulation and theoretical model, Physics of Fluids **37** (2025).

[11] V. M. Boiko, V. P. Kiselev, S. P. Kiselev, A. N. Papyrin, S. V. Poplavsky, and V. M. Fomin, Shock wave interaction with a cloud of particles, Shock Waves **7**, 275 (1997).

[12] J. L. Wagner, S. J. Beresh, S. P. Kearney, W. M. Trott, J. N. Castaneda, B. O. Pruett, and M. R. Baer, A multiphase shock tube for shock wave interactions with dense particle fields, Experiments in Fluids **52**, 1507 (2012).

[13] Y. Ling, J. L. Wagner, S. J. Beresh, S. P. Kearney, and S. Balachandar, Interaction of a planar shock wave with a dense particle curtain: Modeling and experiments, Physics of Fluids **24** (2012).

[14] K. A. Daniel and J. L. Wagner, The shock-induced dispersal of particle curtains with varying material density, International Journal of Multiphase Flow **152**, 104082 (2022).

[15] H. Lv, Z. Wang, and J. Li, Experimental study of planar shock wave interactions with dense packed sand wall, International Journal of Multiphase Flow **89**, 255 (2017).

[16] A. N. Osnes, M. Vartdal, M. G. Omang, and B. A. P. Reif, Computational analysis of shock-induced flow through stationary particle clouds, International Journal of Multiphase Flow **114**, 268 (2019).

[17] P. Zhang, H. Zhang, Y. F. Zhang, S. Li, and Q. Meng, Modeling particle collisions in moderately dense curtain impacted by an incident shock wave, Physics of Fluids **35** (2023).

[18] T. G. Theofanous, V. Mitkin, and C. H. Chang, The dynamics of dense particle clouds subjected to shock waves. part 1. experiments and scaling laws, Journal of Fluid Mechanics **792**, 658 (2016).

[19] E. P. DeMauro, J. L. Wagner, S. J. Beresh, and P. A. Farias, Unsteady drag following shock wave impingement on a dense particle curtain measured using pulse-burst piv, Physical Review Fluids **2**, 064301 (2017).

[20] E. P. DeMauro, J. L. Wagner, L. J. DeChant, S. J. Beresh, and A. M. Turpin, Improved scaling laws for the shock-induced dispersal of a dense particle curtain, Journal of Fluid Mechanics **876**, 881 (2019).

[21] H. Mo, F. S. Lien, F. Zhang, and D. S. Cronin, A mesoscale study on explosively dispersed granular material using direct simulation, Journal of Applied Physics **125** (2019).

[22] J. L. Wagner, S. P. Kearney, S. J. Beresh, E. P. DeMauro, and B. O. Pruett, Flash x-ray

measurements on the shock-induced dispersal of a dense particle curtain, Experiments in Fluids **56**, 213 (2015).

[23] J. Li, K. Xue, J. Zeng, B. Tian, and X. Guo, Shock-induced interfacial instabilities of granular media, Journal of Fluid Mechanics **930**, A22 (2022).

[24] K. Kandan, S. N. Khaderi, H. N. G. Wadley, and V. S. Deshpande, Surface instabilities in shock loaded granular media, Journal of the Mechanics and Physics of Solids **109**, 217 (2017).

[25] V. Rodriguez, R. Saurel, G. Jourdan, and L. Houas, External front instabilities induced by a shocked particle ring, Physical Review E **90**, 043013 (2014).

[26] K. Xue, L. Miu, J. Li, C. Bai, and B. Tian, Explosive dispersal of granular media, Journal of Fluid Mechanics **959** (2023).

[27] L. Miao, J. Li, and K. Xue, Multiscale understanding of structural effect on explosive dispersal of granular media, Journal of Fluid Mechanics **999**, A46 (2024).

[28] P. Wang, T. Pähtz, K. Luo, and Y. Guo, Dispersive wave propagation in disordered flexible fibers enhances stress attenuation, Physical Review E **111**, 015412 (2025).

[29] K. Desmond and S. V. Franklin, Jamming of three-dimensional prolate granular materials, Physical Review E **73**, 031306 (2006).

[30] Y. Bhosale, N. Weiner, A. Butler, S. H. Kim, M. Gazzola, and H. King, Micromechanical origin of plasticity and hysteresis in nestlike packings, Physical Review Letters **128**, 198003 (2022).

[31] Y. Guo, C. Wassgren, J. S. Curtis, and D. Xu, A bonded sphero-cylinder model for the discrete element simulation of elasto-plastic fibers, Chemical Engineering Science **175**, 118 (2018).

[32] Y. Guo, Q. Liu, Y. Li, Z. Li, H. Jin, C. Wassgren, and J. S. Curtis, Discrete element method models of elastic and elastoplastic fiber assemblies, AIChE Journal **67**, e17296 (2021).

[33] C. J. Greenshields, H. G. Weller, L. Gasparini, and J. M. Reese, Implementation of semi-discrete, non-staggered central schemes in a colocated, polyhedral, finite volume framework, for high-speed viscous flows, International Journal for Numerical Methods in Fluids **63**, 1 (2010).

[34] Y. Guo, Y. Li, Q. Liu, H. Jin, D. Xu, C. Wassgren, and J. S. Curtis, An investigation on triaxial compression of flexible fiber packings, AIChE Journal **66**, e16946 (2020).

[35] K. D. Kafui, C. Thornton, and M. J. Adams, Discrete particle-continuum fluid modelling of gas–solid fluidised beds, Chemical Engineering Science **57**, 2395 (2002).

[36] H. Xiao and J. Sun, Algorithms in a robust hybrid cfd-dem solver for particle-laden flows, Communications in Computational Physics **9**, 297 (2011).

[37] L. Zhou, H. Ma, Z. Liu, and Y. Zhao, Development and verification of coarse-grain cfd-dem for nonspherical particles in a gas–solid fluidized bed, AIChE Journal **68**, e17876 (2022).

[38] R. Di Felice, The voidage function for fluid-particle interaction systems, International Journal of Multiphase Flow **20**, 153 (1994).

[39] A. Hölzer and M. Sommerfeld, New simple correlation formula for the drag coefficient of non-spherical particles, Powder Technology **184**, 361 (2008).

[40] D. J. Carlson and R. F. Hoglund, Particle drag and heat transfer in rocket nozzles, AIAA Journal **2**, 1980 (1964).

[41] S. F. Hoerner, *Fluid-Dynamic Drag: Practical Information on Aerodynamic Drag and Hydrodynamic Resistance* (1965).

[42] K. Suzuki, H. Himekl, and T. Watanuki, *Experimental studies on characteristics of shock wave propagation through cylinder array* (Institute of Space and Astronautical Science, 2000) p. 676.

[43] Y. Mehta, C. Neal, K. Salari, T. L. Jackson, S. Balachandar, and S. Thakur, Propagation of a strong shock over a random bed of spherical particles, Journal of Fluid Mechanics **839**, 157 (2018).

[44] Y. Zhao, J. Barés, and J. E. Socolar, Yielding, rigidity, and tensile stress in sheared columns of hexapod granules, Physical Review E **101**, 062903 (2020).

[45] Y. Jung, T. Plumb-Reyes, H. Y. G. Lin, and L. Mahadevan, Entanglement transition in random rod packings, Proceedings of the National Academy of Sciences **122**, e2401868122 (2025).

[46] J. Hao, Y. Li, Y. Liu, J. S. Curtis, and Y. Guo, Jamming in granular shear flows of frictional, polydisperse cylindrical particles, Advanced Powder Technology **32**, 3746 (2021).

[47] P. Han and K. Xue, Shock attenuation of dense granular media, Journal of Fluid Mechanics **1009**, A22 (2025).

[48] J. D. Dietz and R. S. Hoy, Two-stage athermal solidification of semiflexible polymers and fibers, Soft Matter **16**, 6206 (2020).

[49] H. Arkın and W. Janke, Gyration tensor based analysis of the shapes of polymer chains in an attractive spherical cage, The Journal of Chemical Physics **138**, 055101 (2013).